nature electronics

Article

https://doi.org/10.1038/s41928-025-01509-9

A wireless subdural-contained brain–computer interface with 65,536 electrodes and 1,024 channels

Received: 21 March 2025

Accepted: 22 October 2025

Published online: 8 December 2025

Check for updates

A list of authors and their affiliations appears at the end of the paper

Electrocorticography uses non-penetrating electrodes embedded in flexible substrates to record electrical activity from the surface of the brain. To use the technology to develop minimally invasive, high-bandwidth brain–computer interfaces, it will be necessary to improve the number of recording channels and the scalability of devices, which could be achieved by merging electrodes and electronics onto a single substrate. Here we report a 50-µm-thick, mechanically flexible micro-electrocorticography brain–computer interface that integrates a 256 × 256 array of electrodes, signal processing, data telemetry and wireless powering on a single complementary metal–oxide–semiconductor substrate. The device contains 65,536 recording electrodes, from which we can simultaneously record a selectable subset of up to 1,024 channels at a given time. Our chip is wirelessly powered, and when implanted below the dura, it can communicate bidirectionally with an external relay station outside the body. We show that the device can provide chronic, reliable recordings for up to two weeks in pigs and up to two months in behaving non-human primates from the somatosensory, motor and visual cortices, decoding brain signals at high spatiotemporal resolution.

In electrophysiology, a fundamental trade-off exists between the invasiveness of the recording device and the spatiotemporal resolution and signal-to-noise ratio characteristics of the acquired neural signals. Non-invasive techniques, such as electroencephalography, do not require surgery but can only capture limited spatiotemporal dynamics of brain activity[1]. Recording from penetrating electrodes, in contrast, can resolve extracellular action potentials from individual neurons[2,3], but invasive microwires can cause tissue damage[4,5] and compromise long-term recording stability[6,7].

Electrocorticography (ECoG) is an intracranial approach that uses non-penetrating electrodes embedded in thin, flexible substrates that conform to the curvilinear surface of the brain. ECoG records population-level signals, averaged across local neurons. Importantly, because the electrodes sit on the cortical surface, ECoG minimizes brain tissue damage and can acquire higher signal-to-noise ratio, higher bandwidth and more spatially localized signals than electroencephalography[8]. In vivo studies have shown that ECoG recordings taken from subdural arrays can remain stable for more than a year[9,10], illustrating the potential of the technology in chronic applications.

Advances in microfabrication techniques also continue to improve the spatial resolution of the ECoG electrode array. Current leading-edge micro-ECoG (µECoG) arrays provide more than a thousand recording sites with a submillimetre electrode pitch on a single substrate[11,12]. Such progress is encouraging since higher-spatial-resolution µECoG has been shown to improve the accuracy of sensory[13], motor[14] and speech decoding[15]. It has also enabled a more precise mapping of epileptiform waveforms[12] and the recording of neural spiking activity[16].

Yet, current leading-edge high-resolution, multichannel implantable electrodes remain separate from the electronics required for signal conditioning and data transmission. Traditionally, long percutaneous cables have been used to connect the implant to external rack-mount electronics[17–19], but the use of cables restricts the movement of subjects and increases the risk of infection and tissue damage[20,21].

e-mail: tolias@stanford.edu; shepard@ee.columbia.edu

Recently, wireless electronics have been implemented to mitigate these concerns, by either using short percutaneous connection to a wearable headstage[22–24] or implementing a fully subcutaneously integrated system[25–27]. However, current multichannel, high-bandwidth wireless electronics rely on the assembly of discrete, often commercial off-the-shelf components that lead to bulky form factors[22–27], which complicate surgical placement, removal and revision[28,29]. Combining discrete components also results in suboptimal electrical performance compared with what is achievable with application-specific integrated circuits (ASICs) and is hindered by limited interconnect density. This often becomes the bottleneck constraint on the number of recording channels and the scalability of these devices.

To implement the densest neural implants, electrodes and electronics need to be merged onto a single substrate. This has been the key to the success of Neuropixels[17], which features penetrating neural electrodes capable of simultaneously recording from several hundred channels, with each probe equipped with thousands of electrodes and a wired connection to the probe. In this Article, we report a device that monolithically integrates a 256 × 256 high-resolution μECoG electrode array with front-end analogue electronics, an on-chip controller, wireless powering, a radio-frequency transceiver and antennas onto a single complementary metal–oxide–semiconductor (CMOS) substrate[30]. For recording, the device, which is termed a bioelectronic interface system to the cortex (BISC), includes front-end circuitry for signal amplification and filtering and a back-end analogue-to-digital converter. BISC also supports stimulation by including programmable bipolar constant-current sources. Our entire device is a 12 × 12-mm^2 chip whose total thickness is rendered to be less than 50 μm after die thinning and passivation, giving the device enough mechanical flexibility to follow the contour of the brain.

This miniaturization of function allows the BISC chip to be inserted under the dura on the pial matter using relatively simple and efficient surgical procedures, including the ability to replace chips at the same recording location after months, if necessary. Wireless powering and bidirectional communication are provided by a wearable device positioned directly outside the skin over the implant site. We call this device a relay station (Fig. 1a) because it wirelessly powers and communicates with the BISC implant and is capable of being an 802.11n Wi-Fi device itself.

We illustrate the recording fidelity and long-term stability of our device through a series of in vivo experiments on porcine and non-human primate (NHP) subjects. We implant the device over multiple anatomical areas of the cortex and demonstrate high-quality chronic recording and accurate decoding of somatosensory, motor and visual information. From macaque visual cortex recording, our device captured complex spatiotemporal patterns of stimuli-induced travelling waves with spatial features on the scale of a few hundred micrometres and decoded stimulus orientation at a rate of 45 bits per second.

BISC implant form factor

A key metric for implantable brain–computer interface (BCI) devices is 'volumetric efficiency', a measure of functional capability per unit of tissue displaced by the implant. Key to the volumetric efficiency of the BISC system is the chip, which constitutes the entire implanted system (Fig. 1b–d and Supplementary Fig. 1). This chip integrates a 256 × 256 microelectrode array with a pitch of 26.5 × 29 μm, yielding a total array area of 6.8 × 7.4 mm^2 (Fig. 1d,e). Each 14 × 14-μm^2 electrode is composed of titanium nitride (TiN), fabricated via additional microfabrication steps that follow the standard CMOS foundry process (Methods and Supplementary Figs. 3–5). As part of this 'post-processing', the silicon substrate is also thinned to less than 25 μm. Combined with the back-end metal stack, the total chip thickness becomes approximately 40 μm (Fig. 1c and Supplementary Fig. 1b,d). Polyimide is used to encapsulate the front side and parylene, the back side, resulting in a total device thickness of less than 50 μm. The final device has a bending stiffness of approximately 130 μN m, and flexes to a radius of curvature of about 1 mm for a strain of 1% if crystalline defects are minimized during thinning.

A fully processed BISC device has a total volume of 7.2 mm^3 and includes 65,536 electrodes, from which up to 1,024 channels can be recorded simultaneously. Here we define volumetric efficiency as the number of simultaneously recording channels per unit implant volume (Fig. 1f and Supplementary Table 2) and compare our work with other state-of-the-art wireless BCIs. Since the implant volume establishes device invasiveness, we exclude the external relay station from calculation, although some comparison systems integrate its functionality into the implant. Owing to its fully integrated architecture, the BISC achieves over 400 times improvement in volumetric efficiency over the closest competitor. Additionally, our head-mount relay station, which maintains a short-range data link with the implant, offers distinct advantages including wireless uplink bandwidths over 100 times higher than any comparison system and keeping the implant power within safe limits.

BISC implant ASIC design

In the absence of any on-chip compression during recording, the number of simultaneous recording channels and the sampling rate are constrained by the uplink data bandwidth budget of 108 Mbps. To utilize the coverage and density of all the 65,536 available recording electrodes and to preserve the ability to capture the full temporal dynamics of neural activity, we designed our device to digitize and transmit from a spatially programmable subset of either 256 channels at 33.9 kS s^{-1} or 1,024 channels at 8.475 kS s^{-1}.

Every group of 2 × 2 neighbouring electrodes in the array share the same recording pixel circuitry, resulting in 16,384 total pixels. When recording from 256 channels, the active subset can be programmed to any rectangle of 16 × 16 pixel^2, provided that their horizontal and vertical addresses are uniformly spaced. In this mode, only one of the four electrodes from each pixel is recorded. When recording from 1,024 channels, the same 16 × 16 pixel^2 addressing constraint applies, but now recording is taken from all four electrodes in each pixel (Methods and Supplementary Discussion 1).

Each pixel performs signal amplification, chopping and anti-aliasing filtering, and contains the associated digital logic to control these functions and occupies an area of only 53 × 58 μm^2 (Supplementary Fig. 6). This constrained area prevents the implementation of capacitor-based filtering[31], servo-loop-feedback-based or high-dynamic-range direct-quantization-based circuit topologies[32] generally used to prevent saturation in the presence of electrochemical d.c. offsets. We instead rely on the use of TiN electrodes, known to form non-Faradaic, capacitive interfaces[33] to reduce electrochemical d.c. offsets. Electrochemical impedance spectroscopy characterization confirms these properties for the BISC electrodes across the frequency range from 0.1 Hz to 1 MHz with an impedance magnitude of 205 kΩ at 1 kHz, which is equivalent to an electrode capacitance of approximately 0.77 nF (Extended Data Fig. 1a and Supplementary Fig. 4).

Instead of a traditional amplifier, the BISC pixel implements an integrator to provide area-efficient anti-aliasing filtering from boxcar sampling principles[34] with an effective cut-off frequency of 15.1 kHz (Extended Data Fig. 1b and Supplementary Figs. 6 and 15). The use of an integrator also helps to mitigate open-loop gain variation across pixels (Extended Data Fig. 1c). All active pixels are time-multiplexed to share a single back-end programmable gain amplifier (PGA) through which a common gain is configured for all active pixels (Extended Data Fig. 1b and Supplementary Figs. 7 and 15). For high-pass filtering, all the pixels implement a variable pseudo-resistor that is globally configured (Extended Data Fig. 1d and Supplementary Figs. 6 and 15). Input-referred noise integrated from 10 Hz to 4 kHz was measured to be 7.68 μV$_{r.m.s.}$ and 16.51 μV$_{r.m.s.}$ when recording from 256 and 1,024 channels, respectively (Extended Data Fig. 1e,f and Supplementary

https://doi.org/10.1038/s41928-025-01509-9

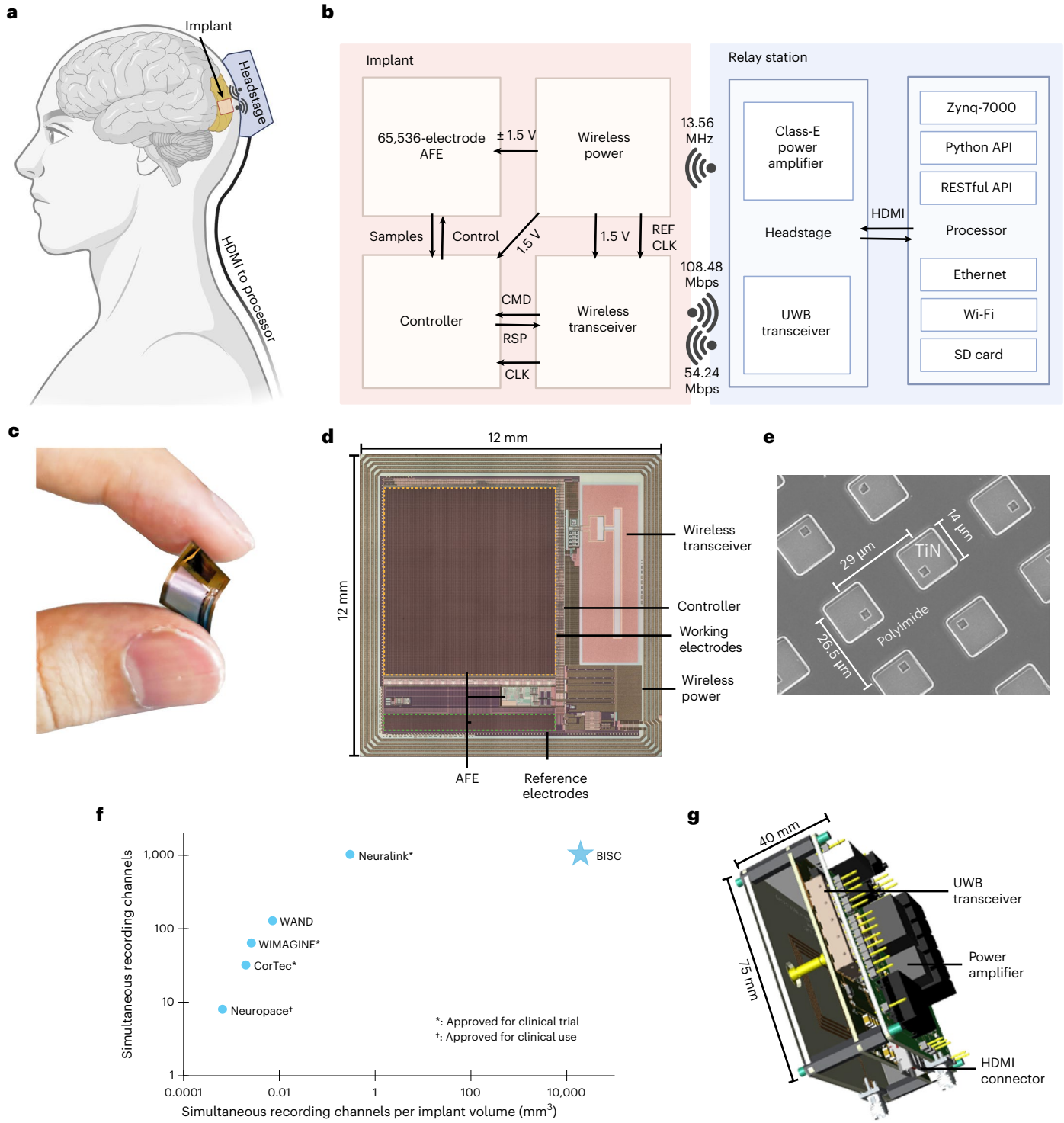

Fig. 1 | BISC implant and relay station. a, Concept diagram of a BISC implant and a relay station. The relay station's headstage provides wireless power and bidirectional communication from outside the body. The headstage module connects to the processor module (not shown) via an HDMI cable. **b**, Schematic of the overall system. The implant has four main modules: an analogue front-end (AFE) for recording and stimulation, wireless power for power transfer through an inductive link, a wireless transceiver for bidirectional data telemetry and a controller for AFE configuration and data packetization. Data move between the headstage and processor modules, with the processor module controlled by a computer through wired or wireless connections using Python/RESTful APIs. **c**, Mechanical flexibility of the BISC implant. **d**, Layout of the BISC implant. **e**, Scanning electron microscopy image of the implant's TiN electrodes. **f**, Comparison of our work with other competing wireless BCI devices. **g**, Three-dimensional diagram of the headstage. Panel **a** created with BioRender.com.

Discussion 3), with more than 90% of the channels functional for a typical device (Extended Data Fig. 1c,f).

The PGA output is digitized with a pair of interleaved 10-bit successive-approximation-register analogue-to-digital converters running at 8.68 MS s^{-1}. Ten samples of the digitized data are grouped into a 125-bit packet by the on-chip controller (Supplementary Discussion 2). The non-data bits in the packet are used for synchronization and error correction coding (Supplementary Fig. 12). The transceiver has uplink and downlink data rates of 108 Mbps and 54 Mbps, respectively, and supports time-division duplexing with a single on-chip antenna by

https://doi.org/10.1038/s41928-025-01509-9

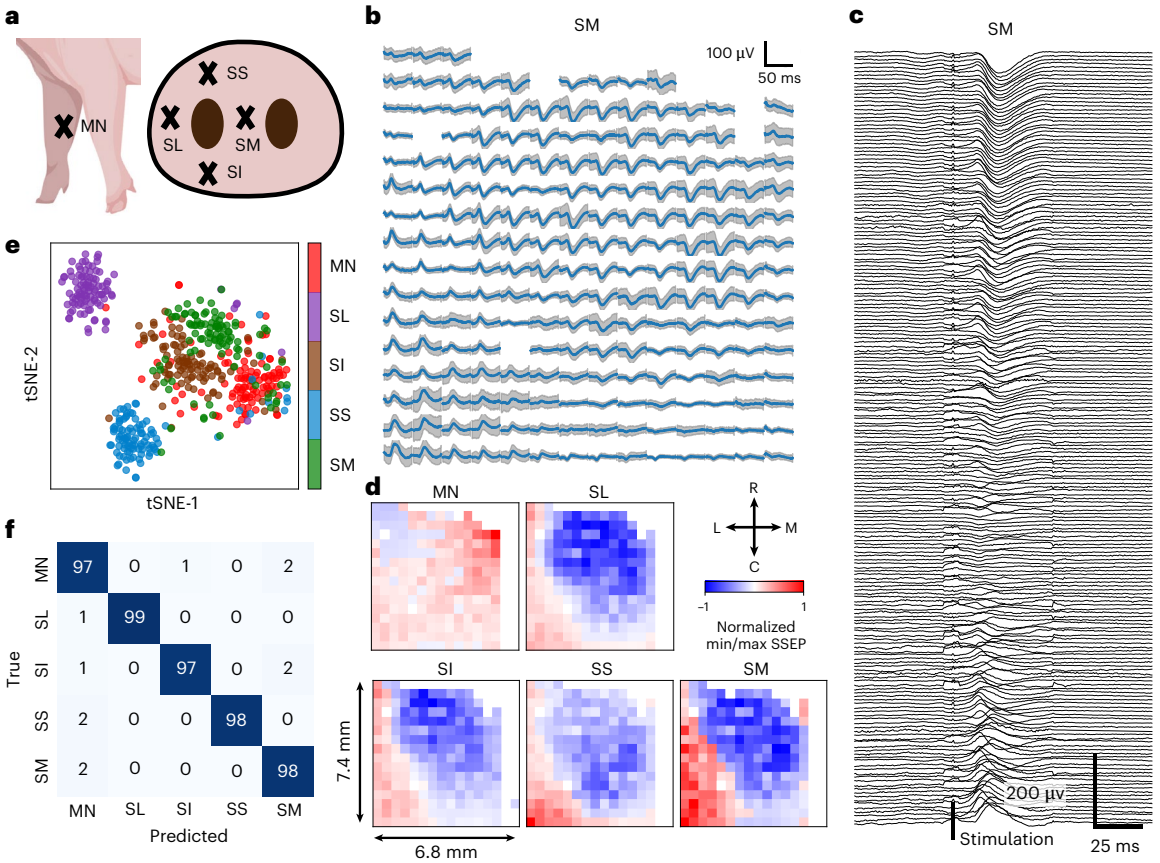

Fig. 2 | BISC recordings over somatosensory cortex from a porcine model. **a**, Location of stimulation (MN, median nerve; SS, snout superior; SL, snout lateral; SI, snout inferior; SM, snout medial). **b**, Example of a stimulation-induced SSEP from 256 channels at 33.9 kS s^{-1} from the full array, trial averaged ($n = 100$). The blue curves indicate the mean; the shaded area indicates the s.d. **c**, Representation of the mean responses in **b** aligned on a shared time axis. **d**, Spatial map of the normalized SSEP extrema. A positive value indicates that the peak SSEP magnitude was greater than the trough magnitude. A negative value indicates that the trough SSEP magnitude was greater than the peak magnitude. The cross indicates orientation of the implant in **b** and **d** (R, rostral; C, caudal; L, lateral; M, medial). **e**, State-space representation of the SSEPs using *t*-distributed stochastic neighbour embedding (tSNE; $n = 100$ per location). **f**, Prediction of stimulation location using a linear discriminant classifier ($n = 100$ per location). Panel **a** created with BioRender.com.

utilizing a transmit/receive switch (Supplementary Discussion 1 and Supplementary Fig. 9).

Wireless power transfer utilizes a near-field inductive coupling at 13.56 MHz (Supplementary Discussion 1 and Supplementary Figs. 10 and 11). This choice of frequency keeps the specific absorption rate below 2 W kg^{-1} (refs. 35,36; Supplementary Fig. 11). The system clock of the implant is derived from the wireless power transfer carrier, eliminating the need for an on-implant crystal oscillator. The BISC implant consumes less than 64 mW of total power, satisfying the thermal budget guideline of 0.5 mW mm^{-2} for neural implants[37,38] (Supplementary Fig. 11).

Relay station design

The relay station wirelessly powers the implant and transfers data between the BISC chip and a computer base station. It is a two-part system that consists of a headstage and a processor module (Fig. 1b and Methods), designed from commercial off-the-shelf components.

The headstage has a wearable form factor (75 × 75 × 45 mm^3, 151 g) with printed circuit boards (PCBs) that include a custom powering coil and an ultrawideband (UWB) antenna (Fig. 1g and Supplementary Fig. 2). Data telemetry uses an impulse-radio UWB transceiver centred at 4 GHz with on–off-keying modulation, linking a dipole antenna on the headstage to a monopole antenna on the implant.

The processor module powers and configures components on the headstage, sends queries and commands to the implant, and receives responses and recorded data from the implant. It combines a microprocessor running the Linux operating system with programmable logic that manages neural data streaming and executes time-sensitive command sequences (Supplementary Fig. 13). A graphical user interface running on a computer base station communicates with the processor module through RESTful application programming interface (API; Supplementary Fig. 14), allowing users to configure the recording parameters and display real-time neural data.

Surgical approaches for the implant

The thin, mechanically flexible form factor of the BISC implant enables relatively simple surgical implantation compared with any device using penetrating intracortical electrodes or percutaneous connections. In both pig and NHP models, a standard craniotomy on the scale of 25 mm × 23 mm was made adjacent to the implantation site (Supplementary Discussions 5 and 9). The dura was then carefully elevated using sutures or forceps and linearly cut to provide a clear path for implantation. A commercial strip electrode was used as the insertion shuttle (Supplementary Fig. 17), with the sterilized BISC chip placed on top and inserted under the dura, resting the implant directly on the pial surface. Importantly, the dural incision was made adjacent to the implantation site to avoid cuts or sutures directly over it. Once the chip is positioned, the dura was sutured, the skull was repositioned and the incision was closed.

This procedure also supports easy upgrading or replacement of the BISC chip. After several months of implantation in an NHP, we reopened the skull, made a new dural incision over the previous one and replaced the chip in less than 10 min. This rapid, safe and

effective upgrade process offers a substantial advantage over other invasive BCI systems, where device replacement is more complex and time-consuming.

Somatosensory evoked potential in porcine model

In vivo studies reported in this paper have focused on the recording capabilities of BISC. Our device was first subchronically validated by implantation over a porcine somatosensory cortex. Two weeks after the implant, we recorded somatosensory evoked potentials (SSEP) from the anaesthetized animal in response to peripheral stimulation (Supplementary Discussion 5). Five weeks after implantation, the whole brain was extracted post-mortem for histological examination (Supplementary Fig. 19).

For the SSEP recordings, percutaneous electrical stimulations were delivered to the median nerve and four distinct locations of the snout (Fig. 2a), which is known to have a large somatotopic representation in the pig brain[39]. The recording was taken from 16 × 16 channels, configured in the sparsest mode that covers the whole array. Data from these channels were low-pass filtered (300 Hz, eight-order Butterworth, zero phase), subtracted by their baselines, and then downsampled to 2.11 kS s^{-1} (Supplementary Discussion 6). Trial-averaged channel responses (Fig. 2b,c and Supplementary Fig. 18) show wave complexes whose peak polarization and depolarization timings are similar to those found in previous studies[40]. The spatial arrangement of the normalized peak response (Fig. 2d and Supplementary Video 1) is also consistent with the previously reported somatotopy[39,41].

The fidelity of SSEP recordings was assessed by visualizing in two dimensions and building a classification model. In both analyses, we first used principal component analysis to reduce the z-scored spatiotemporal waveforms into a lower-dimensional space, retaining components that explained 80% of the variance. These extracted components were projected onto a two-dimensional space using t-distribution stochastic neighbour embedding[42]. This projection (Fig. 2e) results in clearly separable clusters, indicating that the measured SSEP can be used to effectively distinguish between peripheral stimulation sites. The decoding performance was quantified using a linear discriminant model with tenfold cross-validation that resulted in an overall accuracy of 97.8 ± 1.7% (mean ± standard deviation (s.d.), n = 500; Fig. 2f).

Coronal sections were collected from the post-mortem extracted brain for histological analysis using three markers: haematoxylin and eosin, NeuN, and Iba1 (Supplementary Fig. 19). Sections taken directly from under the BISC implant showed no noticeable pathology by haematoxylin and eosin or NeuN. Iba1, however, revealed a mild microgliosis extending from the superficial cortex to the subcortical white matter. Near the perimeter of our device, there was a small lesion on the surface of the cortex, consistent with a mechanical injury incurred during insertion by the commercial-strip-electrode shuttle. No pathological changes were seen in sections taken as control samples from the occipital cortex.

Motor cortex recording in NHP

Before the chronic NHP study, the BISC device was validated through acute recordings using a glass artificial skull mounted in a permanent craniotomy and durotomy (4 cm × 2 cm) over the motor cortex region of a behaving NHP subject[43]. In this setup, the glass module is hermetically secured to a base ring affixed to the subject's skull using mechanical screws, eliminating the need for additional surgery for device implantation. The subject was seated in a primate chair, facing the experimenter who manually held a wand at the subject's full-reach distance. The subject was trained to asynchronously reach, grab the wand and then retract its arm without the use of an explicit cue to prompt its movement, with the arm location triangulated from multiple cameras (Fig. 3a and Supplementary Discussion 7).

For this experiment, the BISC device was attached directly to the artificial skull (Fig. 3b) and positioned over the central sulcus (CS), with most electrodes over the primary motor cortex (M1) but a substantial portion over the primary somatosensory cortex (S1; Fig. 3c).

As the subject was performing the behavioural task, BISC recordings were taken from 16 × 16 channels configured in the sparsest mode covering the whole array. The fidelity of the measured local field potentials (LFPs) was assessed by building a continuous velocity decoder using a linear model (Fig. 3d–f and Supplementary Discussion 8) and visualizing the spatiotemporal dynamics of selected frequency bands (Fig. 3g,h).

The decoder was built by first identifying channels (n = 180 out of 256) that consistently remained non-saturated throughout the experiment. Data from these channels were band-pass filtered (0.3 to 300 Hz) and downsampled to 2.11 kS s^{-1}. Recordings contained a strong haemodynamic rhythm around 3 Hz, which we associated with the heart rate (180 beats per minute). This rhythm was removed by subtracting the corresponding time-series components computed through space–time singular value decomposition[44] (Supplementary Fig. 20). The preprocessed recordings were further grouped into four frequency bands: local motor potential (LMP), β (10 to 30 Hz), low γ (30 to 70 Hz) and high γ (70 to 190 Hz). Low-frequency LMP was extracted by applying boxcar averaging with a 50-ms window and then z-scoring[45]. The other three bands were extracted by applying multitaper estimation with a 200-ms window and 10-Hz half-bandwidth and then normalizing[46]. Finally, the time history of features from (t − 0.47) s to (t + 0.47) s in 52-ms time steps were used for decoding, resulting in a 13,680-dimensional vector $X(t)$ (180 channels, 19 time lags and 4 frequency bands) as the model input for decoding the motor feature $y(t)$.

We decoded the arm velocity using partial least squares (PLS) regression because it is effective in handling data whose predictor is highly correlated and has a large dimension compared with the number of observations[47]. The optimal number of PLS components was determined by calculating the minimum predictive error sum of squares across fivefold cross-validation (Supplementary Fig. 20). When decoded against the normalized y dimension (front–back) wrist velocity, feature prediction resulted in Pearson's correlation coefficient of 0.53 ± 0.04 (mean ± standard error), illustrated by an example time segment shown in Fig. 3e. Spectral contributions to the decoder from each frequency band were found by computing the sum of the relative weight of coefficients associated with each band (Fig. 3f).

The two bands with the highest contributions—LMP and high-γ band—are further visualized by plotting their multichannel power over time (Fig. 3g), which shows fluctuations synchronized to the subject's motion. Spatiotemporal progression of these bands in a selected 1-s-long time window (Fig. 3h) shows spatially localized activity in both M1 and S1, with LMP displaying patterns that resemble phase reversal across the CS boundary. A more detailed version of this plot with a finer time resolution and an extended time range is provided in Supplementary Video 2.

Visual cortex recording in NHP

The stability of chronic neural signals from the BISC implant was validated through long-term (up to 64 days) studies from the visual cortex of an adult macaque monkey. The chip was placed near the V1–V2 border, partially covering V4 as well (Fig. 4a). Over the span of the study, we conducted multiple experiments that involved three different visual stimulus paradigms: gratings, random dots and natural images.

In the grating sessions, the monkey fixated for at least 300 ms to initiate a trial in which 30 static gratings of random orientations were consecutively presented (Fig. 4b). Each grating lasted 50 ms. The BISC recordings were taken from 16 × 16 channels configured in the sparsest mode covering the whole array. Approximately one-third of them, primarily those overlying V1, showed an increased response for the Fourier components between 20 Hz and 90 Hz (Fig. 4c). The peaks at 20 Hz and harmonics in the power spectrum response reflect the grating changing every 50 ms. We selected four example channels labelled by their chip

https://doi.org/10.1038/s41928-025-01509-9

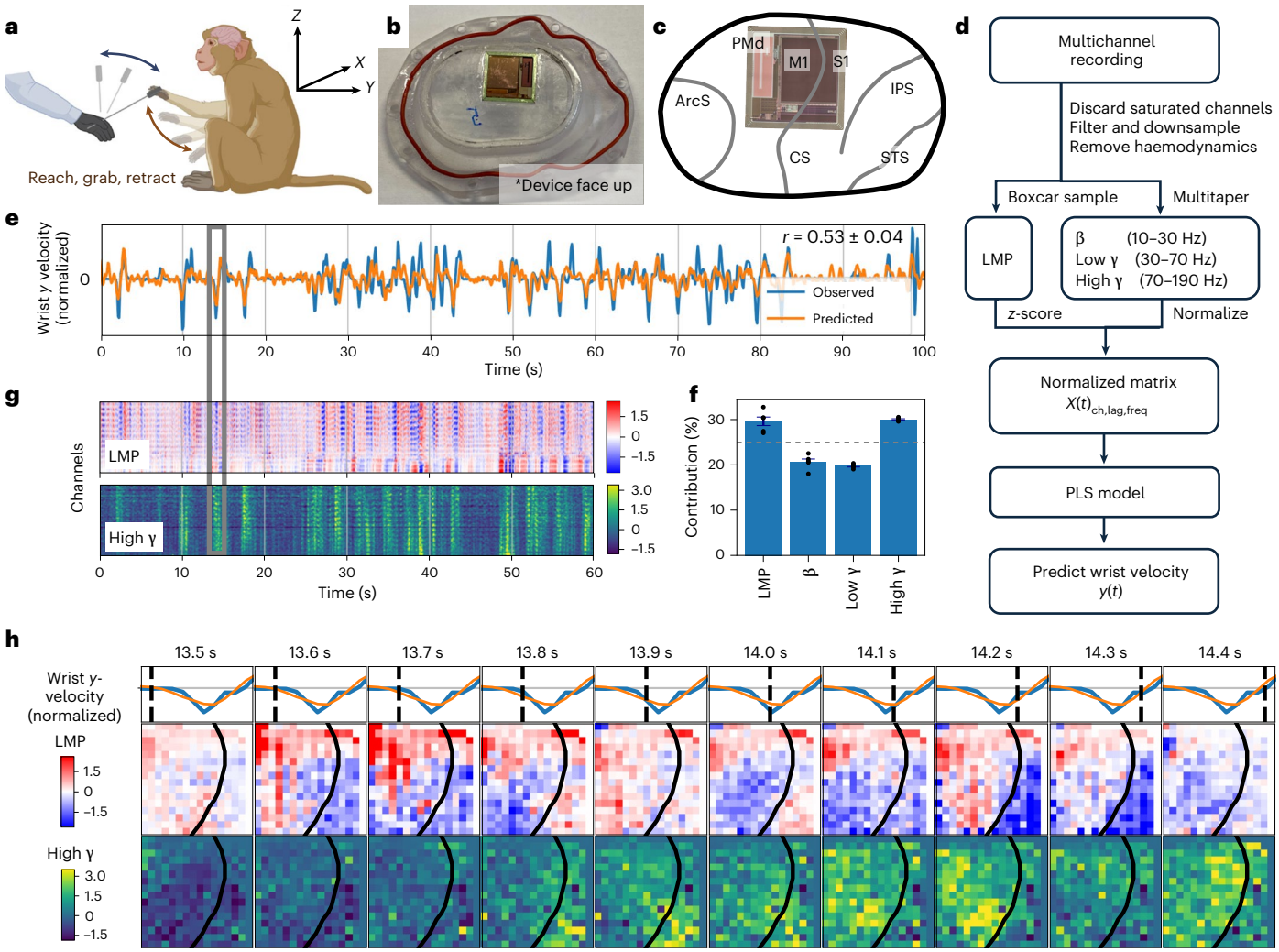

Fig. 3 | BISC recordings over motor cortex from a behaving NHP. a, Behavioural task depiction. The subject was trained to asynchronously reach and grab a 'wand' held by the experimenter without an explicit cue. **b**, Device placement on the artificial skull. **c**, Registration of the device with respect to the brain surface anatomy. **d**, Motor feature decoding pipeline. A linear PLS regression model uses a spatial–temporal–spectral input $X(t)$ to predict the subject's motor feature $y(t)$. **e**, Representative example of the continuous decoding of normalized wrist velocity in the y direction (front–back). **f**, Spectral contributions to the decoder from each frequency band. Bars indicate the mean, the error bars indicate the standard error, and the dashed line denotes the chance level. Individual data points ($n = 5$ cross-validation folds; 3,420 samples per fold) are overlaid as black dots. **g**, Representative example of the spatiotemporal dynamics of LMP and high-γ band, both z-scored. The time axes in **e** and **g** are shared. **h**, Representative example of a frame-by-frame spatiotemporal progression of LMP and high-γ band, both z-scored. The plotted time window is indicated by the vertical grey box over **e** and **g**. The dashed lines indicate the time instants of each frame, and the solid curves over the frames represent the CS in **c**. Recordings are taken from 256 channels at 33.9 kS s^{-1} from the full array. Panel **a** created with BioRender.com.

coordinates (Fig. 4d) to show their band-pass-filtered responses in one trial (Fig. 4e). It is evident that the activity in these channels is elicited by the onset of the visual stimulus and returns to the baseline after the stimulus. We further applied Morlet wavelet transformation (Supplementary Discussion 10) to acquire the spectrogram of each channel. The averaged spectrogram of one channel after aligning at the stimulus onset is shown (Fig. 4f), along with six individual bands with central frequencies evenly spaced on a logarithmic scale (Fig. 4g). We observed different responses in each band, defined as the ratio of the mean response in the time window from 500 to 1,500 ms relative to the stimulus onset over the mean response in the time window from −300 to 0 ms. The resulting response maps are shown for multiple bands (Fig. 4h).

For each frequency band, we computed the grating-triggered average response by aligning the response segments according to the grating onset and obtained the average band-pass-scaled response conditioned on each grating orientation (Supplementary Discussion 10). The result contains a strong untuned component corresponding to the grating switching (Supplementary Fig. 21). After its removal, the residual components show that the channel responses during the time window from 50 to 200 ms after grating onsets are tuned to the grating orientations. A typical channel is shown in Fig. 4i. We take the average response between 88 and 112 ms after grating onset to measure each channel's tuning curve and define the orientation selectivity index as the difference between its maximum and minimum values. Orientation selectivity index maps across multiple frequency bands are shown in Fig. 4j. Tuning curves for the 64-Hz band are shown in Fig. 4k. Channels exhibiting pronounced tuning and higher orientation selectivity indices correspond to those overlying V1. As expected, we observe strong orientation tuning in the gamma (γ) band.

We then built an orientation decoder from these responses, which takes raw responses (with no filtering) of all channels in the time window from 0 to 200 ms after grating onset and returns a distribution of grating orientations. We trained the decoder as a classifier in which the orientation is discretized into 36 bins. The decoder is a multilayer

convolutional neural network (CNN) that uses one-dimensional convolution along the temporal dimension. The performance on a hold-out set (containing trials not used during training) is shown in Fig. 4l. The mutual information $I(\theta; r) = H(\theta) - H(\theta|r)$ between the predicted orientation θ and BISC responses r is computed to be approximately 2.27 bits, corresponding to a data rate of 45 bits per second at a 50-ms frame rate (Supplementary Discussion 10 and Supplementary Figs. 24 and 25). The decoder prediction closely approximates the ground-truth values (Fig. 4m), with a root mean squared error of 9.1° (Fig. 4n).

We mapped the spatial receptive fields (RFs) using a random dot experiment, where single 0.51° dots appeared on a uniform grey background, changing the location and colour (black/white) every 50 ms (Fig. 5a). Dots were presented within a 6° × 6° rectangular field, centred 1.5° right and 3° below fixation. The monkey maintained fixation for 1,500 ms to receive a juice reward. After removing the Fourier components outside the 20-to-90-Hz band, the band-passed responses for all non-saturated channels are shown for one trial (Fig. 5b).

We computed the RF by dot-triggered averaging on wavelet-transformed responses. Multiple wavelet central frequencies were tested (Supplementary Videos 3–8) and almost all of them show a clean structure for channels in the V1 area. An example channel is shown in Fig. 5c for the 64-Hz band. This channel is responsive to a dot shown in the lower-right location ~40–80 ms after dot onset. By averaging the spatiotemporal RF over time, we compute an estimate of the spatial RFs, which are shown with a shared colour scale (Fig. 5d). Although channels in V1 have compact RFs, the presented dot size is too small to invoke a spatially structured response from the channels outside V1. We fit two-dimensional Gaussian functions to these spatial RFs and plot the retinotopic map using the fitted Gaussian centres (Fig. 5e). We examined the chronic stability of these maps by comparing them from day 36, days 41–48 and day 62 post-surgery. The RFs remained stable, showing average changes of less than 0.05° in eccentricity and less than 2.7° in angle for all channels from day 36 to day 62 for both dense (days 41–48) and sparse (days 36 and 62) recordings, demonstrating the stability of chronic BISC recordings (Fig. 5f).

To exploit the fine-pitch 65,536-electrode structure of the BISC chip, we densely recorded (minimum electrode pitches at 26.5 µm × 29 µm) from the top-left quadrant of the electrode array through repeated, contiguous recording blocks of 1,024 channels. The combined results (Fig. 5g) are consistent with the findings in the sparse full-array recordings and provide a retinotopic map with a much higher resolution.

The spatially dense recordings from the BISC implant also capture fine-grained spatiotemporal dynamics of LFPs that cannot be resolved in the sparse configuration. Specifically, in the BISC recordings, we observe 'travelling waves'—spatiotemporally coherent patterns of propagating neural oscillations—consistent with recent findings showing that such waves can encode task-related spatial information[48]. We focused on identifying travelling waves in the γ band (30–90 Hz), given the task-related oscillations in this range (Fig. 4f–j). To measure the γ-band travelling waves, we extracted the instantaneous phase of the γ oscillation at each channel in the dense configuration. Then, we measured the topography of the γ travelling waves, using circular statistics to extract the instantaneous direction and strength of the γ phase gradient at each contact (Supplementary Discussion 10). With this approach, we compared the strength of the γ travelling waves across dense recordings taken from 16 different locations of the array during dot viewing. The strongest travelling waves were recorded from the top-left corner of the BISC array, corresponding to posterior medial recordings over the operculum in V1 (Fig. 6a(i), red outline). Our subsequent analysis (Fig. 6a(ii),b–e) focuses on recordings from this section of the array.

First, we compared the spatial topographies of travelling waves induced by dot stimuli (Fig. 6a), revealing distinct cortical patterns that varied with the dot location in the visual field. To assess whether BISC's spatially dense recordings revealed additional stimulus-relevant information not present in the lower-density recordings, we used uniform manifold approximation and projection (UMAP) clustering analysis on responses to five example dot locations (Supplementary Discussion 10). Spatially dense BISC recordings more effectively distinguished wave patterns across dot locations compared with lower-resolution measurements (Fig. 6b).

To further test whether travelling waves encoded information about dot locations across the visual field, we built a neural network decoder to predict the horizontal and vertical coordinates of the dot viewed by the monkey based on the spatiotemporal pattern of the BISC-measured travelling waves. This decoder uses a hybrid neural network architecture, including a CNN that assesses the topography of travelling waves at each moment and a transformer network to extract long-range temporal correlations. The model was trained by using the spatiotemporal sequence of travelling waves from each trial to predict the current dot location viewed by the monkey (Fig. 6c, Supplementary Discussion 10 and Supplementary Video 9). We used this

Fig. 4 | BISC recordings over visual cortex with grating stimuli. a, Chip position on the cortex. The chip was implanted on the border between the V1 and V4 areas. Note that a mirrored image is used here as the chip is facing down. **b**, Trial in the grating session. The monkey is required to fixate for at least 300 ms before visual stimuli are presented on the monitor. Thirty static gratings with random orientations are displayed in one trial, each lasting 50 ms. **c**, Spectrum comparison between fixation period and stimulus period. Fourier transform is applied to responses in the time window between −300 and 0 ms (blue) and the time window between 500 and 1,500 ms (red) relative to the grating stimulus onset. The solid lines are averaged over channels and trials and the shaded areas mark the standard deviation of the trial average over channels. **d**, Channel coordinates in the full-chip recording mode. We simultaneously record 256 channels at 33.9 kS s^{-1} from the full chip. **e**, Filtered responses of example channels. For 4 channels that are strongly responsive to grating stimuli, responses after removing the Fourier components below 20 Hz and above 90 Hz for 1 trial are shown. The vertical lines indicate the onset of stimulation. **f**, Trial-averaged spectrogram of one channel. We applied wavelet transformation on the recorded signal and obtained the time-varying power for different frequency bands. **g**, Temporal profiles of the selected frequency bands. Six rows from **f** are plotted as solid lines. The shaded area denotes the standard error of the mean across trials. The grey background marks the period in which the grating stimuli are presented. **h**, Responsiveness maps of different bands. Responsiveness for each channel in the given frequency bands is defined as the signal power during the time window from 500 to 1,500 ms divided by that during −300 to 0 ms. **i**, Orientation tuning of an example channel. We computed the grating-triggered average response conditioned for each orientation. The simple average contains a strong orientation-independent component that reflects the switching of grating every 50 ms (Supplementary Discussion 9). The heat map shows the orientation-tuned components after the removal of the orientation-independent component. **j**, Orientation selectivity maps of different bands. The orientation selectivity index is defined based on the tuned response during the time window from 88 to 112 ms after grating onset (Supplementary Discussion 10). **k**, Orientation tuning curves of all channels from the 64-Hz band. The tuned response averaged over the time window from 88 to 112 ms as a function of the grating orientation is shown for all channels. The unit of each channel's response is the standard deviation σ across trials computed during the fixation period. **l**, Orientation decoder performance. We trained a decoder that takes raw responses from all channels in the time window from 0 to 200 ms after grating onset, and predicts the grating orientation. The decoder outputs a distribution over orientations. The average decoder output is shown for each orientation on a hold-out testing set of trials. Mutual information between the prediction and response is computed after discretizing the orientation into 36 bins. **m**, Point estimation on the testing set. A circular mean of the decoder outputs is computed as point estimations. **n**, Histogram of prediction error. The difference between point estimation and ground truth is gathered for all gratings in the testing trials. Brain rendering in **a** adapted with permission from ref. 71, Elsevier and ref. 72, Springer Nature Limited.

https://doi.org/10.1038/s41928-025-01509-9

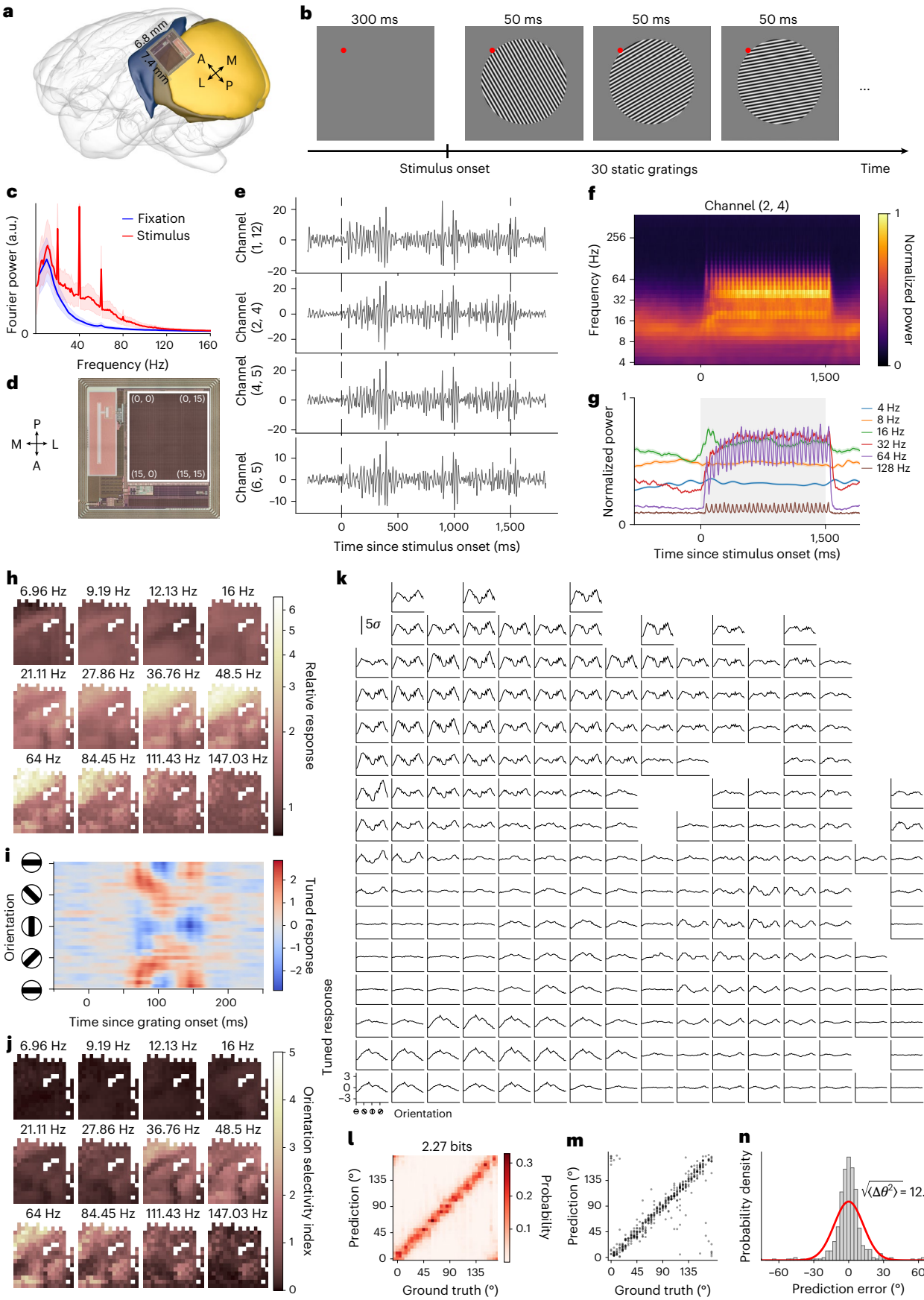

https://doi.org/10.1038/s41928-025-01509-9

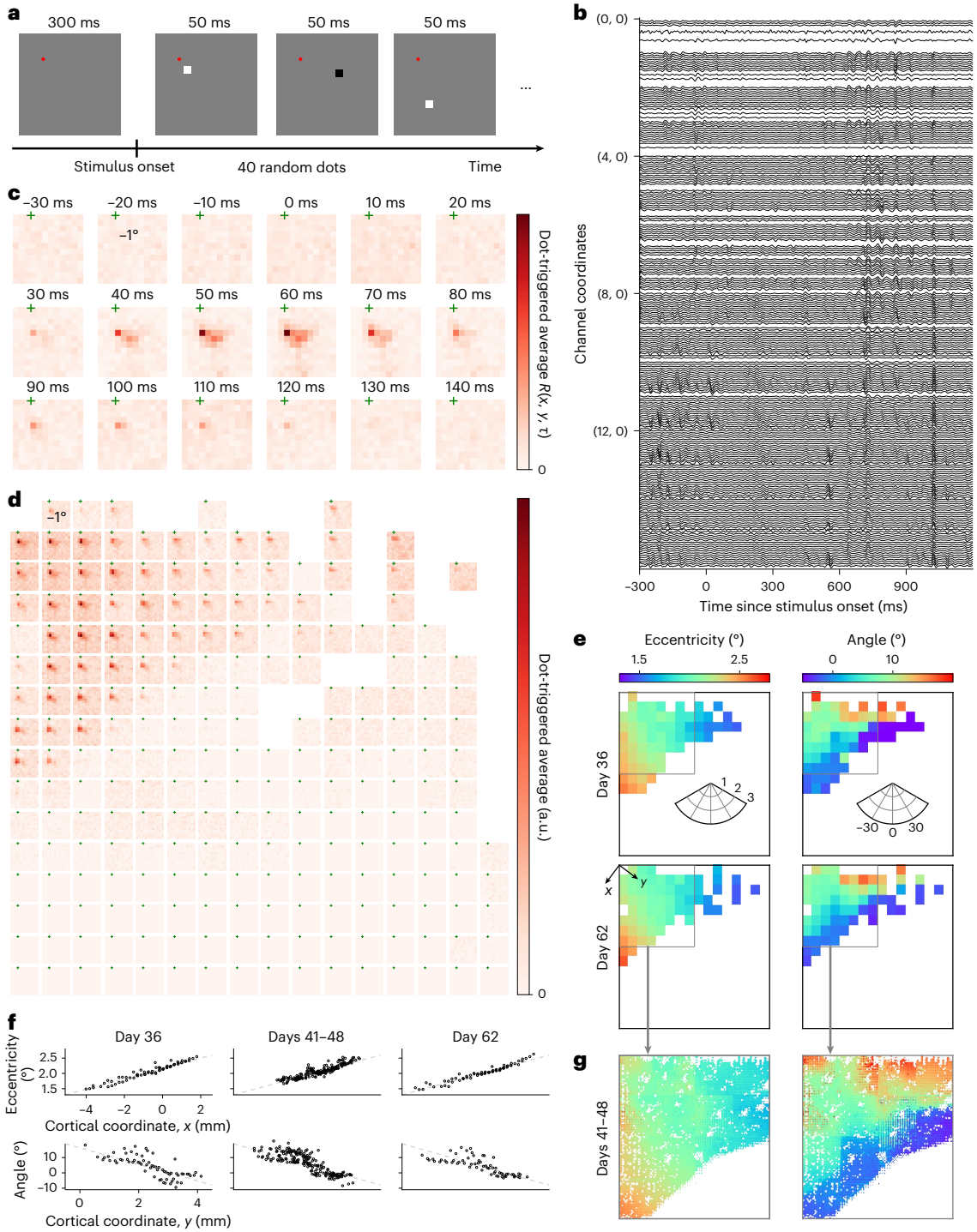

Fig. 5 | BISC recordings over visual cortex with dot stimuli. a, Trial in the dot-mapping session. Forty random dots of either black or white colour are shown within the visual field region [−1.5°, 4.5°] × [0°, 6°] (horizontal × vertical), each lasting 50 ms. **b**, Filtered response of all non-saturated channels from a full-chip recording session. We show their responses after removing the Fourier components below 20 Hz and above 90 Hz for 1 trial. **c**, Spatiotemporal RF of one example channel. We filtered the response by a Morlet wavelet of which the central frequency is 64 Hz, and computed the dot-triggered average of the signal power. Times are relative to dot onset and the cross symbol represents the fixation location. **d**, Spatial RF of all non-saturated channels. The spatial RF is computed by taking the temporal average of the dot-triggered average responses. **e**, Chronic stability of retinotopic maps (recording electrode pitch approximately 440 µm). A two-dimensional Gaussian fit is computed for the spatial RF of each channel separately, and we take the fitted centre as the RF centre. Channels with a good Gaussian fit (fraction of unexplained variance smaller than 0.8) are shown for recordings from day 36 and 62 after surgery. **f**, RF locations projected on the cortical axes on day 36, days 41–48 and day 62 after surgery. We denoted the direction along which the RF eccentricity changes the fastest on the chip as '*x*', and the orthogonal direction as '*y*'. The RF centres are plotted against the channel projections on *x* and *y* separately. Overall, the eccentricity changes roughly at the rate 0.17 visual degree per millimetre. Across days, the RF changed by less than 0.05° in eccentricity and less than 2.7° in angle on average for all the channels for both dense (days 41–48) and sparse (days 36 and 64) recordings, demonstrating the stability of BISC chronic recordings. **g**, Higher-resolution retinotopic map (recording electrode pitch, ~28 µm) from the upper-left quarter of the chip. We performed 16 dense recording sessions over 8 days, with 1,024 channels simultaneously recorded in each session.

network to assess the statistical robustness of dot-specific travelling waves over time and compared the decoding accuracy across different recording resolutions.

Using the sequence of γ-band travelling waves observed in each trial, our model could reliably decode the coordinates of individual dots, with the highest accuracy for dots near the centre of the visual field (Fig. 6d). The decoding accuracy is significantly higher with full-resolution BISC recordings compared with lower-resolution recordings (Fig. 6e, full resolution versus quarter resolution: two-sided *t*-test, $t(285) = 2.7$, $P = 7.7 \times 10^{-3}$).

To assess the temporal dynamics of travelling waves, we next tested whether dot decoding depends not only on the current travelling wave pattern but also on the recent history of waves and stimuli. This hypothesis was tested by shuffling the sequence of past dot presentations and the corresponding wave patterns, and then using the model to decode the dot location from waves immediately following this shuffled sequence. The shuffling led to a significant drop in decoding accuracy (Fig. 6e, two sided *t*-test, $t(220) = 2.0$, $P = 4.6 \times 10^{-2}$), indicating that the recorded travelling waves reflect both current stimuli and recent histories of stimuli and cortical activity[49], which is extracted by the CNN and transformer network.

Last, we examined the nonlinear response characteristics of BISC recording channels when exposed to coloured natural images (Extended Data Fig. 2a). In this paradigm, the fixating monkey was shown a large number of coloured natural images from the ImageNet database[50]. In each of the five recording sessions with sparse recording over the entire array of 16 × 16 channels, 10,000–12,000 unique natural images were presented in blocks of 15 images, with each image displayed for 120 ms (ref. 51). The images (10° × 10°) were centred at a location 3° to the right and below the fixation spot. We then applied zero-phase component analysis whitening across all the channels and band-pass filtered the signal between 30 and 90 Hz (tenth-order Butterworth, zero phase), followed by squaring and averaging the signal from 40 to 160 ms after image onset. Through these processing steps, we derived a scalar magnitude from the γ band of each channel, known to reflect the spiking activity of the adjacent neuronal population[52], in response to each natural image. We then fit a deep neural network model (Extended Data Fig. 2b) to pairs of natural images and γ-band responses to learn the stimulus-response mapping, that is, a digital twin of each recorded channel, enabling the model to predict the activity of any channel for an arbitrary stimulus. Then, we selected and fine-tuned an ImageNet-pretrained CNN model[53] as a shared feature space, with learned channel-specific weights, to predict the individual channel responses[54]. Next, we tested the accuracy of our digital twin model on a held-out set of 75 natural images. Each image was repeated 40 times and was never shown to the model during training.

As a measure of predictive performance (Extended Data Fig. 2c), we computed the correlation between the model prediction and the averaged neuronal response to repeated presentations of the same test image, which resulted in 0.69 ± 0.14 (mean ± s.d.) across all the selected channels. This is comparable or better than the performance of similar predictive models of isolated single neurons in macaque V1 (ref. 51). Additionally, we computed the explainable variance for each channel, which measures the response reliability to natural images. This metric is defined as the ratio of response variance across repeated presentations of the same image over the response variance across all images (Extended Data Fig. 2c). We only selected channels with an explainable variance larger than 0.1. Across all channels, we obtained an average explainable variance of 0.24 ± 0.09 (mean ± s.d.), slightly below the values of 0.31 and 0.32 that were reported for isolated single neurons in macaque V1 and V4, respectively[51,55]. The spatial distribution of the model performance (Extended Data Fig. 2d) and response reliability (Extended Data Fig. 2e) indicate that channels closer to V1 exhibit higher model performance and response reliability compared with those in higher visual areas. We then visualize the feature selectivity of each channel by using our predictive model (digital twin; Extended Data Fig. 2f). Traditionally, parametric stimuli or hand-designed images are used to investigate the visual feature selectivity of single neurons or populations, with the strongest-evoking stimuli used to determine their tuning functions.

More recently, digital twin models have been used to synthesize optimal stimuli by iteratively optimizing images to maximize the response of a neuron or channel. These optimized stimuli, referred to as maximally exciting images (MEIs), can be thought of as nonlinear RFs[56] that reveal underlying neural functions such as tuning characteristics in mouse V1 (refs. 56–58), as well as monkey V1 (ref. 57) and V4 (refs. 51,59,60). Here we show the MEIs for individual channels to demonstrate their visual feature tuning. Remarkably, the MEIs (Extended Data Fig. 2g) reveal a hierarchy of complexity from area V1 (top left) to V2 (centre) and V4 (bottom right). As expected from MEIs of single V1 neurons[57], V1 is characterized with oriented Gabor filters. V2 and V4 exhibit more complex features with dominant colour opponency (also observed in ref. 59). These results demonstrate that the digital twin model can capture detailed, nonlinear visual response characteristics of the local neuronal population for each recorded channel.

Conclusions

We have developed a BCI system that can be implanted entirely subdurally. Like traditional μECoG arrays, it relies on recording and stimulation

Fig. 6 | Spatially dense BISC recordings over visual cortex capture complex travelling waves that encode the locations of viewed dot stimuli. a, (i) Mean strength of travelling waves at each of the 16 dense recordings taken from subsets of the BISC array during the dot-mapping experiment. These 16 recordings are also presented in Fig. 5g; the red line indicates the V1–V2 boundary identified from the retinotopic map. Recordings over V1 show higher wave strength compared with those over V2, consistent with the enhanced functional role of V1 compared with V2 in processing simple visual features such as dot locations. (ii) Each dot stimulus location evokes a distinct pattern of travelling waves. Travelling wave topographies captured by 1,024-channel, dense recordings taken from the top-left subset of the array shown in **a**(i) (red box) for each of the 5 example dot locations. Travelling waves are estimated from the gradient of the phase of oscillations in the γ band (30–90 Hz) in the 40–90-ms interval relative to the dot onset; this interval was chosen as it evokes the maximum neural response (Fig. 5c). Note the spatial complexity of the travelling waves, with even adjacent dots evoking spatially distinct patterns. **b**, Separation of the travelling wave patterns between different dot locations visualized using UMAP. Low-dimensional UMAP embeddings are shown for four different channel resolutions as defined by the average electrode pitch. Colours indicate the dot stimulus locations. Note that the dot locations are clearly separated in UMAP space for 100% sampling. Separation decreases for spatial sampling at lower resolutions. The separability of dot locations is quantified using the silhouette score, with higher scores reflecting greater separability at a higher spatial resolution (two-sided *t*-test, $t(515) = 4.8$, $^{***}P = 2.1 \times 10^{-6}$). Each bar indicates the mean ($n = 279$), and the error bars indicate the standard error of the mean. **c**, Decoding the dot locations from the travelling waves at the locations shown in **a** using a hybrid CNN-transformer model. The predicted *x* and *y* coordinates closely match the true dot locations, as shown in the accuracy trace plots. **d**, A heat map displays the prediction accuracy for individual dot locations, illustrating the decoding variability across the visual field. Dots presented closer to the centre of the visual field (dark red) exhibit a higher decoding accuracy, matching the RF maps. **e**, Decoding accuracy as a function of the spatial sampling of the BISC channels, showing the importance of the BISC chip's high-density recordings for capturing spatially precise features of travelling waves (full resolution versus quarter resolution: two-sided *t*-test, $t(285) = 2.7$, $^{**}P = 7.7 \times 10^{-3}$). Temporally shuffled controls confirm the temporal dependencies of these high-resolution travelling waves, as shuffling of the order between consecutive stimuli reduces the prediction accuracy for individual dots (two-sided *t*-test, $t(219) = 2.0$, $^{*}P = 4.6 \times 10^{-2}$). Each bar indicates the mean ($n = 144$), and the error bars indicate the standard error of the mean across cross-validation folds.

https://doi.org/10.1038/s41928-025-01509-9

from the surface, but at a dramatically higher electrode density. The advantage this device has over those relying on intracortical electrodes, particularly in the context of eventual human translation, lies in its surgical procedures: its removal and replacement are straightforward, and results in little to no cortical damage. In the future, we expect to transition to even less invasive surgical procedures in which only a small slit is made in the cranium and dura, and the BISC implant is slid under the skull.

Positioning the BISC implant on the pial brain surface allows it to naturally conform to the contour of the brain and move with the brain, bringing advantages over devices with components attached to the skull, which introduce relative motion between the device and the brain. An additional benefit of subdural μECoG recordings over intracortical recordings for clinical translation is their stability over time, which was replicated in the BISC.

The BISC chip was designed with a front-end recording bandwidth sufficient to capture the temporal dynamics of neural spiking activity. Our in vivo experiments did not demonstrate the existence of large-scale spiking activity from BISC surface recordings. Future iterations of BISC that focus only on LFP recordings can reduce the front-end recording bandwidth and better utilize the available 108-Mbps data bandwidth to simultaneously record from a larger number of channels. The architecture of BISC in which full recording circuitry is present at each electrode site allows this scalability. The high-density recording capability of the BISC device shows that even LFPs, when measured with small surface electrodes placed directly on the pial surface, exhibit

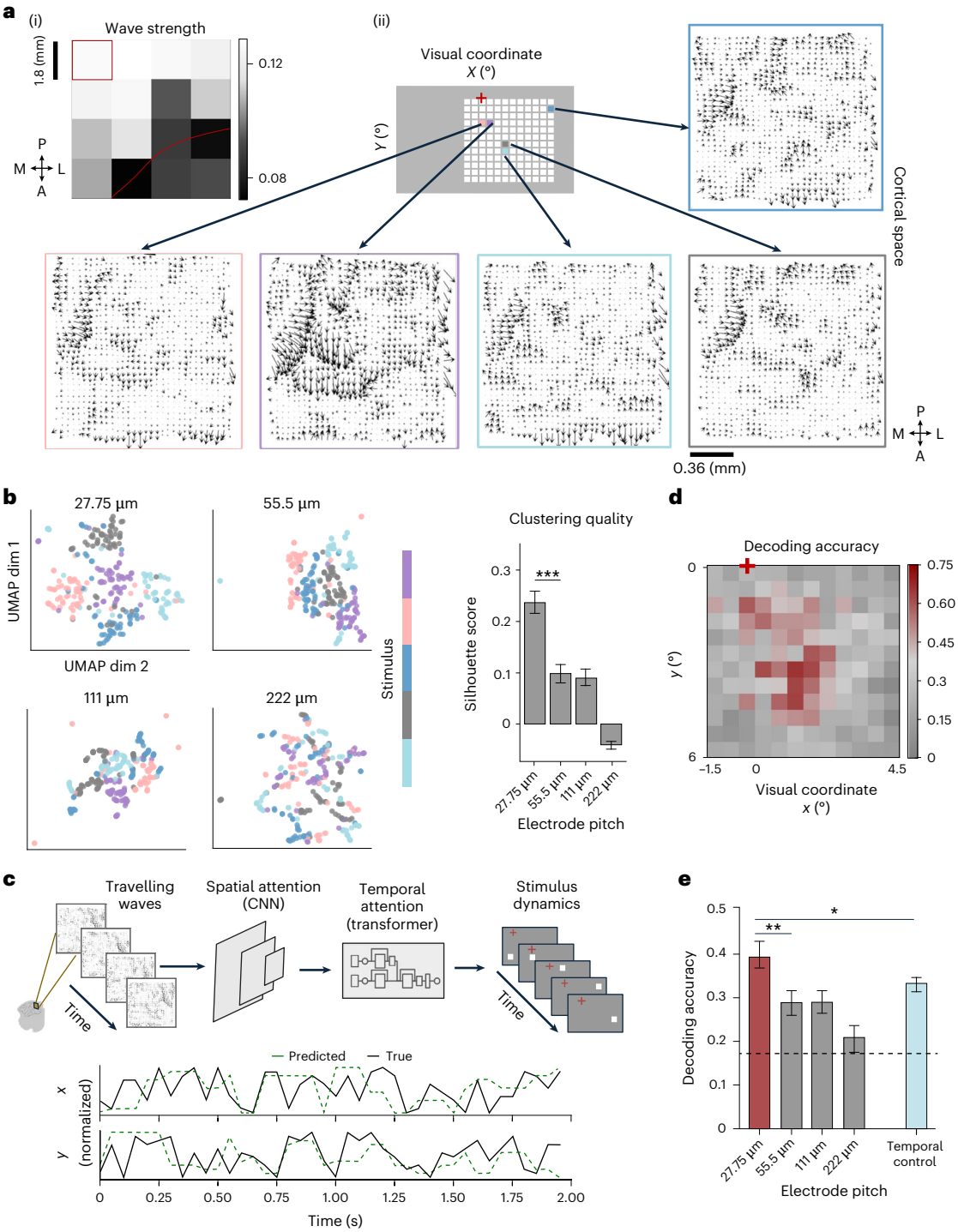

precise spatiotemporal patterns at a scale of tens of micrometres. These patterns convey information about both current and past stimuli, as demonstrated by the decoder performance trained on γ-band travelling waves in the primary visual cortex.

Prior work has measured travelling waves with more widely spaced electrodes in scales of centimetres[61] or millimetres[62], but the BISC is able to record them in the primate brain at a much finer spatial resolution. These travelling waves (Fig. 6a) exhibit patterns that roughly match the spatial scale of orientation pinwheels[63] and individual cortical columns[64].

By measuring the travelling waves at a much finer spatial scale, the BISC provides an opportunity to study how they interact with detailed cortical gradients. Our demonstration of information decoding at a scale of tens of micrometres in V1 raises the question of whether similar high-resolution decoding can be achieved in other brain areas relevant for human BCI applications, such as speech or motor. The feasibility of such applications depends on the topological organization of the local circuits and the underlying task demands.

The BISC chip also supports amplitude-controlled, biphasic current stimulation that can be configured to be either cathodic first or anodic first, followed by a passive balancing phase (Methods and Supplementary Figs. 8 and 15). The stimulation circuits in each of the 16,384 pixels can be independently programmed (Supplementary Discussion 1), limited only by the aggregate current that can be sourced or sinked at any given time. Future experiments with BISC will test these stimulation capabilities.

Although the current version of BISC relies on on-chip electrodes, the BISC electronics can be easily connected to polyimide extenders, which would allow BISC to be adapted for intracortical depth electrodes, large-area surface electrodes or both. These extenders can be attached to BISC through solder-bump attachment, thermosonic bonding or anisotropic conductive films. Multiple BISC devices can also be tiled over the brain surface to achieve larger area coverage without using extenders. These alternatives build on the technology validated in this work: a fully encapsulated, integrated, wireless, bidirectional neural interface that can be placed subdurally and controlled from an antenna outside the scalp. Scalability and modularity of the BISC system allows it to be adapted effectively to meet these diverse applications.

The current headstage design is bulky, limiting its suitability for freely moving animal studies and future human use. Its volume can be reduced by integrating the electronics in the current bill of materials into a single-stack PCB connected to a wearable antenna via dual radio-frequency cables. Further form-factor reductions will come from developing an ASIC that replaces most discrete PCB components.

By delivering volumetric efficiency, BISC overcomes some of the barriers to widespread clinical translation faced by alternative technologies that rely on percutaneous wires or implanted canisters. It is also timely, given recent advances in the performance of BCI systems for speech and motor control[65,66]. Combining BISC's high-density wireless recording and stimulation capabilities with deep learning methods provides a promising direction for future high-bandwidth bidirectional BCIs for the treatment of brain diseases, ranging from depression and aphasia to motor disorders, stroke and blindness.

Methods

BISC implant design

The BISC implant (Supplementary Fig. 1), a custom-designed ASIC measuring 12 mm × 12 mm, was manufactured by the Taiwan Semiconductor Manufacturing Company (TSMC) in a 0.13-µm bipolar–CMOS–double-diffused metal–oxide–semiconductor process (Supplementary Fig. 1). Post-processing steps, including thinning to 25 µm, electrode processing and passivation, were conducted in-house in the semiconductor processing facilities at Columbia University on coupons and at the 200-mm wafer scale at MIT Lincoln Laboratories, as described below.

The implementation of the implant followed a custom mixed-signal design flow. The digital circuits, which include the logic of the on-chip controller, were designed as finite-state machines in SystemVerilog hardware description language. This language was subsequently synthesized into a gate-level description using a logic synthesizer (Genus, Cadence Design Systems), and place and routed using a physical implementation tool (Innovus, Cadence Design Systems) using TSMC's 0.13-µm bipolar–CMOS–double-diffused metal–oxide–semiconductor standard-cell libraries. For the analogue circuit design and implementation, schematic capture and layout tools (Virtuoso, Cadence Design Systems) were used. Radio-frequency and microwave tools (Ansys Electronics Desktop, Ansys; PathWave Advanced Design System, Keysight Technologies) were used for power coil and antenna designs.

The BISC implant features 65,536 surface TiN electrodes in its 16,384-pixel array. We provide a basic overview of the design here, with more details provided in Supplementary Discussion 1. BISC allows a programmable selection of 1,024 or 256 simultaneously recording channels from any of its electrodes with a set of rules.

- Every group of two × two electrodes (a pixel) is connected to an underlying pixel amplifier. Electrodes numbered from 1 to 65,536 are connected to in-pixel amplifiers numbered from 1 to 16,384 (sequentially from left to right and from top to bottom). Electrodes 1, 2, 257 and 258 are connected to pixel amplifier 1, and electrodes 65,279, 65,280, 65,535 and 65,536 are connected to pixel amplifier 16,384.
- A group of 16 × 16 in-pixel amplifiers can be used for each recording configuration. Both vertical and horizontal spacing (stride) of the amplifiers in that group can be programmed individually from 0 to 7 pixels. For example, selecting a group with zero horizontal and vertical spacing (the densest spatial configuration) at the array's top-left corner records from amplifiers 1–16, 129–144…1,921–1,936. By contrast, selecting a group with the maximum spacing (seven horizontal and vertical) results in a configuration with the highest spatial coverage.
- Each electrode in a pixel can be either statically or dynamically multiplexed to the in-pixel neural amplifier. In static multiplexing, 256 channels (1 per pixel) are simultaneously read-out at a sampling rate of 33.9 kS s^{-1}. In dynamic multiplexing, 1,024 channels (four per pixel) are read-out simultaneously at 8.475 kS s^{-1}.

Each electrode is a 14 µm × 14 µm square. In the densest configuration, with the centre-to-centre electrode pitches at 26.5 µm × 29 µm, 32 × 32 electrodes cover an area of 0.85 mm × 0.93 mm. By contrast, the least-dense configuration spaces, the electrodes, are 424 µm × 464 µm apart and 16 × 16 electrodes cover an area of 6.4 mm × 7.0 mm.

The reference input for the in-pixel neural amplifiers can be connected either to column-wise reference electrodes or to a global counter electrode; the latter acts as the ground reference potential for the chip. No substantial differences were observed between these two schemes in our comparative evaluations. Consequently, the counterelectrode reference configuration was used for all experiments conducted.

The in-pixel amplifiers are designed as chopped integrators, with their inputs biased by transistors in the weak-inversion region at the input. To avoid space-consuming d.c.-blocking capacitors, the electrical double layer formed at the non-Faradaic TiN electrodes is used as an implicit d.c. block. The pixel amplifier inputs are biased to 0 V (ground) during operation. Chopping in the in-pixel amplifiers is used to reject intrinsic voltage offset and $1/f$ noise. The pixel amplifier outputs are multiplexed into a single, two-stage PGA. The total voltage gain of the system can be programmed from 484 to 1,620 V V^{-1} and a high-pass corner can be programmed from 4 to 55 Hz. The low-pass corner of the system is 15 kHz. The outputs of the PGA are subsequently digitized by an 8.68 MS s^{-1}, interleaved 10-bit successive-approximation-register analogue-to-digital converter. When recording from 256 channels, the

BISC implant has an input-referred noise of less than 5 $V_{r.m.s.}$ across the frequency range of 10 Hz to 1 kHz and 10 $\mu V_{r.m.s.}$ for the range from 0.3 Hz to 10 kHz. When recording from 1,024 channels, the input-referred noise is less than 8 $\mu V_{r.m.s.}$ from 4 Hz to 1 kHz.

The implant also allows a stimulation current driven from any group of electrodes with a set of rules.

- Stimulation can be driven from a minimum of a single two × two electrode group (a pixel), up to the full array of 65,536 electrodes, acting as a macroelectrode.
- For monopolar stimulation, any combination of macroelectrodes can be used to drive current at a given time.
- For bipolar stimulation, macroelectrodes can be used to drive current either in phase or out of phase. Macroelectrodes driving opposite phases must have equal widths and have the same column addresses, but their heights can be individually programmed.

The temporal profile for stimulation has three phases. The first two phases are anodic or cathodic, generating currents from two on-chip-regulated current sources. During these phases, switches that connect the stimulation electrode to the corresponding current source are activated, allowing the current to flow from the source to the electrodes. Both anodic and cathodic currents have the same amplitude, which is linearly programmable from 10 µA to 1.02 mA. The third phase is for charge balancing, in which the electrodes used for stimulation are grounded to ensure no accumulated charge on the electrodes. The duration of all the three phases can be independently programmed from 0 to 350 µs. The compliance voltages of the anodic and cathodic current sources are ±1.4 V.

The BISC implant has a wireless transceiver with an on-chip slot monopole antenna, enabling wireless communication with the relay station. It operates as a UWB impulse radio, encoding digital data in short 'bursts' of a 4-GHz sine wave. In this encoding scheme, '1' is represented by a burst, whereas '0' is the absence of a burst. The transceiver occupies up to 700 MHz of bandwidth in the unlicensed UWB frequency band and can support uplink data rates of 108.48 Mbps and downlink data rates of 54.24 Mbps. To allow full duplex communication using a single antenna, transmitting and receiving are time-division multiplexed for every bit. This allows us to precisely control the timing to stop a recording and the implant still transmits data to the relay station.

The implant features wireless power transfer that allows harvesting more than 64 mW from the integrated power coil through an inductive resonance coupling. The a.c. power received on the powering coil is first rectified by an active rectifier and then regulated by regulators to support the 1.5-V power domain as three separate rails and one −1.5-V power domain.

Relay station design

The relay station (Supplementary Fig. 2) interfaces the BISC implant to a host computer, providing wireless power to the implant, sending commands to control the implant's operation, collecting recorded data and relaying everything to the host computer over wired or wireless connection. The relay station has two parts: the headstage in which the wireless transceiver and power amplifier reside, and a processor module in which a Xilinx Zynq processor and logic translators reside.

The headstage is a wearable device (75 × 75 × 45 mm^3, 151 g) prototyped using off-the-shelf components and PCBs. It establishes wireless communication with the BISC implant and supplies power to the implant through an integrated wireless transceiver and power amplifier. The headstage is connected to the processor module with a standard HDMI cable, which can be up to 5 m in length. The HDMI cable sends 12-V d.c. power to the power regulators on the headstage, delivering up to 1.2 A. The wireless transceiver on the headstage transmits high-speed digital data up to 108.48 Mbps using low-voltage positive emitter-coupled logic over the differential twisted pairs on the HDMI cable to the processor board. A microcontroller (Teensy 4.1, PJRC) integrated on the headstage configures the wireless transceiver and the power amplifier. Communication between the microcontroller and the processor board is achieved using a two-wire UART protocol through the HDMI cable.

The BISC headstage is assembled by stacking four separate PCBs. The arrangement of the boards, from the bottom (facing implant) to the top, is as follows:

- UWB circular dipole antenna board. A dipole antenna is printed on a 0.2-mm-thick, single-layer FR-4 substrate. It is co-designed with the powering coil to optimize the bandwidth and radiation efficiency. The antenna board connects to the transceiver board with an in-series SMP adaptor (19K104-K00L5, Rosenberger Group). A balun (BD3150N50100AHF, Anaren) is installed on this board to convert the single-ended radio-frequency signal from the SMP adaptor to a differential signal for the dipole.
- Power coil board. The power-transmitting coil is a square spiral, printed on a 1.6-mm-thick, two-layer FR-4 substrate. It is fabricated with 13-oz (0.455-mm-thick) copper to implement a high-Q inductor for enhanced efficiency and minimal heat loss. The coil has an outer diameter of 3.6 cm and an inner diameter of 2.5 cm to allow clearance for the UWB dipole antenna. The coil has an effective impedance of 885 nH and 1.1 Ω with a self-resonance frequency well beyond (>70 MHz) the link frequency. The measured link efficiency is −10.5 dB at 1.5-cm distance, assuming an ideal conjugate-matched driving source and a 75-Ω load at the receiver side, which is equivalent to the overall circuit load. The coil is terminated with an edge-launch SMA connector and is driven by the power amplifier board via a short (75-mm) SMA cable.
- Transceiver board. The transceiver board is a 1.6-mm-thick four-layer PCB. Rogers RO4003C is used as the top prepreg to allow good impedance matching and reduce power loss, whereas FR-4 is used as the core and bottom prepreg to lower the cost. Components installed on the transceiver board are for transmitting and receiving UWB pulses. The SMP connector to the antenna board, receiving chain and transmitting chain are connected through a single-pole-double-throw radio-frequency switch (HMC8038, Analog Devices). In the receiving chain, the radio-frequency signal first passes through a digitally controlled attenuator (HMC540SLP3E, Analog Devices) to prevent electromagnetic interference saturating the amplifiers. Subsequently, the signal is amplified 60 dB using two low-noise amplifiers (CMD308P4, Qorvo) in series and filtered by a band-pass filter (B040MB5S, Knowles). An envelope detector (ADL6012, Analog Devices) then extracts the envelope of the incoming signal, followed by a threshold detector comprising two operational amplifiers (THS4304, Texas Instruments) and a comparator (TLV3604, Texas Instruments). The threshold detected signal becomes a digital short pulse if the implant is transmitting a 1 or stays constant if transmitting a 0. Multipath fading or reflection in the transmitting path can cause spurious pulses to be detected by the threshold detector. This issue is resolved by using a self-resetting edge detector, which waits for 6 ns between detections to allow echoes to decay, and resets the outputs after each detection. The edge detector is built from a low-voltage positive emitter-coupled logic buffer (SY89327L, Microchip Technology), a D-flip flop (SY10EP51VMG, Microchip Technology) and a comparator (TLV3601, Texas Instruments). The final output from the edge detector is fed into a divide-by-2 divider (MC100EP32, Onsemi), converting the digital pulses into a non-return-to-zero data stream. This stream is then sent over the HDMI cable (receiver) and sampled by the field-programmable gate array, and the original data are reconstructed by XORing the current

and previous received bits. In the transmitting chain, a frequency synthesizer (ADF4351, Analog Devices) is used to generate the 4-GHz sine-wave bursts. To transmit a 1, the processor board sends a logic high through the HDMI cable (transmitter), and the radio-frequency output from the synthesizer is activated, driving the dipole antenna via the radio-frequency switch. The reference clock of the synthesizer and control signal for the radio-frequency switch are also sent over the HDMI cable (CLK and TR) by the processor board. Additionally, this board houses the microcontroller that controls the attenuator and the reference voltage of the threshold detector. The d.c. power, reference clock and other control signals are passed to the power amplifier board via a board-to-board connector.

- Power amplifier board. The power amplifier board implements a class-E amplifier to drive the power coil at 13.56 MHz. The amplifier uses a single-ended gallium nitride transistor (EPC2051, Efficient Power Conversion) as the active switch, loaded with a standard matching network[67] that shapes the impedance of the coil. In an inductively coupled system, the link efficiency and tuning of its resonant frequency depend on a number of dynamic variables such as the coil-to-coil alignment, electromagnetic properties of the environment, operating mode of the implant and so on. To compensate for these variables in real time, the board uses two feedback mechanisms to keep the link operating at its optimum. First, it controls the radiation magnitude by periodically reading out the level of power received by the implant and adjusting the supply voltage of the class-E amplifier through an inter-integrated circuit configurable regulator (TPS65400, Texas Instruments). Second, it prevents detuning of the resonance by adjusting the series capacitance of the load network using a reconfigurable capacitor bank[68]. By monitoring the current consumed by the class-E amplifier under different load conditions, the 4-bit (1-pF least significant bit) bank is configured to keep the link resonance stable at 13.56 MHz.

The processor module is based on a platform (Snickerdoodle Black, Krtkl) that runs both firmware and the Linux operating system on the field-programmable gate array and ARM processor of a Zynq-7020 system on a chip. We designed APIs using Python language and Xilinx PYNQ libraries. Our Python software running on Linux (Ubuntu 18.04) provides methods to fully control the BISC implant, stream the recording data over the ethernet or store it on a secure digital card, as well as control the microcontroller on the BISC headstage.

The BISC relay station presently only works with one implant at a time. However, multiple devices can be implanted if a spacing of at least 5 mm is maintained between devices. In this scheme, an implant would be selectively powered up by positioning the headstage over it.

BISC implant post-processing

Coupon processing. A coupon consisting of four reticles (total dies, 16) was scribed out from the original 300-mm BISC wafer from TSMC using a diamond scribe. Supplementary Fig. 3 shows a schematic of the process flow through a cross-section of the microelectrode array region. A layer of photoresist (AZ P4620, MicroChemicals) was spin coated onto the coupon at 3,000 rpm, exposed on a contact mask aligner (MA-6, Karl Suss) and then developed (AZ 400K, MicroChemicals). Etching the silicon oxide and nitride layers with a plasma etcher (Oxford Instruments) exposed the Al redistribution layer at the electrode sites. The redistribution layer was wet etched in an Al etchant (Type A, Transene) to expose the underlying Ta diffusion barrier layer over the redistribution via layer. A brief Ar-ion sputter to remove the Ta oxide layer was followed by sputtering 240 nm of TiN (120 min, 0.33 Å s^{-1}, 20 s.c.c.m. Ar, 3 mtorr, 175 W) on Ta in the same vacuum chamber (Orion 8 Dielectric Sputter Chamber, AJA International), and the resist was lifted off using a photoresist remover (Remover PG, Kayaku).

TiN was chosen as the electrode material due to its biocompatibility, rough surface morphology providing a reduction in impedance (Z = 205 kΩ at 1 kHz for a 14 µm × 14 µm electrode) compared with a smooth electrode material such as gold (Z = 3.1 MΩ at 1 kHz for a 14 µm × 14 µm electrode), strong adhesion for chronic implantation and stimulation, compatibility with CMOS processing and capacitive non-Faradaic current properties[69]. Supplementary Fig. 4 shows the characterizations of BISC TiN electrodes.

After electrode fabrication, a 2.5-µm-thick polyimide encapsulation layer (PI2610, HD Microsystems) was spin coated onto the front surface after functionalizing the surface with an adhesion promoter (VM652, HD Microsystems) and cured at 350 °C for 30 min, followed by spin coating a layer of photoresist (AZ P4620, MicroChemicals). The TiN electrodes were exposed using oxygen-plasma etching (Oxford Instruments). After a brief Ar-ion clean, a second 360-nm TiN layer was sputtered on top of the first TiN layer using the same deposition parameters, and the AZ P4620 mask was lifted off in Remover PG. Each die was then separated with a dicing saw (DISCO Corporation) and bonded frontside down on a glass carrier using an instant adhesive (LOCTITE 460, Henkel) for thinning on a grinding and polishing tool (X-Prep, Allied High Tech) to a final silicon substrate thickness of ~25 µm. Chips were then loaded into a parylene-coating chamber (Specialty Coating Systems) to encapsulate the backside with 10 µm of parylene C. The parylene was trimmed along the edge to leave about a 1-mm overhang for handling and the chip was released from the glass carrier by dissolving the adhesive in acetone.

Wafer-scale processing. Whole eight-inch wafers can be processed in a similar way starting with the TiN electrode fabrication and polyimide front-surface encapsulation. Assuming the entire wafer is dedicated to BISC chips, a single wafer yields up to 200 fully contained devices ready for sterilization and implantation (Supplementary Fig. 5).

During mechanical thinning, grinding-induced defects are introduced into the silicon, which can serve as nucleation sites for bending-induced fracture growth and device failure. Extensive polishing is needed to remove these defects. With this in mind, for the wafer-scale thinning process, we developed a wet-etch thinning technique using an isotropic silicon etch consisting of hydrofluoric, nitric and acetic acids. The device wafer was bonded to a silicon carrier wafer using an organic adhesive (WaferBond HT-10.11, Brewer Science). The wafer edges were clamped using an O-ring seal, and the wafer surface was covered in an etchant, which was stirred and maintained at room temperature to give a uniform etch rate of 4.28 µm min^{-1} across the wafer. The remaining silicon thickness was monitored during etching, and the wafer was removed and rinsed in deionized water once this value reached 25 µm.

The chips were carefully aligned using features visible through the thinned backside of the wafer and singulated by laser dicing (DISCO Corporation) through the thinned wafer with 100-µm-wide dicing lanes, stopping within the WaferBond adhesive layer. A 10-µm-thick film of parylene C was deposited onto the backside of the wafer in a room-temperature chamber (Specialty Coating Systems) using an adhesion promoter (Silane A174, Sigma-Aldrich). The wafer was then loaded into an excimer laser dicing tool (IPG Photonics) and was aligned as before. Parylene within the dicing lanes was laser cut with a dicing width of 60 µm to leave a 20-µm overhang of parylene along the chip edges. The wafer was then submerged in a WaferBond remover (1-dodecene, Brewer Science) to dissolve the underlying adhesive. The individual chips were collected and rinsed in acetone and isopropanol and dried with nitrogen.

Reporting summary

Further information on research design is available in the Nature Portfolio Reporting Summary linked to this article.

Data availability

All electrophysiological data relevant to the figures presented in this paper are available via GitHub at https://github.com/klshepard/bisc with a version archived in Zenodo (https://doi.org/10.5281/zenodo.17074065)[70]. All other relevant data are available from the corresponding authors upon reasonable request.

Code availability

All scripts used for the data analysis are available via GitHub at https://github.com/klshepard/bisc. All other relevant codes are available from the corresponding authors upon reasonable request.

References

1. Biasiucci, A., Franceschiello, B. & Murray, M. M. Electroencephalography. *Curr. Biol.* **29**, R80–R85 (2019).
2. Nicolelis, M. A. L., Ghazanfar, A. A., Faggin, B. M., Votaw, S. & Oliveira, L. M. O. Reconstructing the engram: simultaneous, multisite, many single neuron recordings. *Neuron* **18**, 529–537 (1997).
3. Maynard, E. M., Nordhausen, C. T. & Normann, R. A. The Utah Intracortical Electrode Array: a recording structure for potential brain-computer interfaces. *Electroencephalogr. Clin. Neurophysiol.* **102**, 228–239 (1997).
4. Polikov, V. S., Tresco, P. A. & Reichert, W. M. Response of brain tissue to chronically implanted neural electrodes. *J. Neurosci. Methods* **148**, 1–18 (2005).
5. Salatino, J. W., Ludwig, K. A., Kozai, T. D. Y. & Purcell, E. K. Glial responses to implanted electrodes in the brain. *Nat. Biomed. Eng.* **1**, 862–877 (2017).
6. Rousche, P. J. & Normann, R. A. Chronic recording capability of the Utah Intracortical Electrode Array in cat sensory cortex. *J. Neurosci. Methods* **82**, 1–15 (1998).
7. Chestek, C. A. et al. Long-term stability of neural prosthetic control signals from silicon cortical arrays in rhesus macaque motor cortex. *J. Neural Eng.* **8**, 045005 (2011).
8. Volkova, K., Lebedev, M. A., Kaplan, A. & Ossadtchi, A. Decoding movement from electrocorticographic activity: a review. *Front. Neuroinform.* **13**, 74 (2019).
9. Nurse, E. S. et al. Consistency of long-term subdural electrocorticography in humans. *IEEE Trans. Biomed. Eng.* **65**, 344–352 (2018).
10. Yan, T. et al. Chronic subdural electrocorticography in nonhuman primates by an implantable wireless device for brain-machine interfaces. *Front. Neurosci.* **17**, 1260675 (2023).
11. Chiang, C.-H. et al. Development of a neural interface for high-definition, long-term recording in rodents and nonhuman primates. *Sci. Transl. Med.* **12**, eaay4682 (2020).
12. Tchoe, Y. et al. Human brain mapping with multithousand-channel PtNRGrids resolves spatiotemporal dynamics. *Sci. Transl. Med.* **14**, eabj1441 (2022).
13. Kaiju, T. et al. High spatiotemporal resolution ECoG recording of somatosensory evoked potentials with flexible micro-electrode arrays. *Front. Neural Circuits* **11**, 20 (2017).
14. Wang, P. T. et al. Comparison of decoding resolution of standard and high-density electrocorticogram electrodes. *J. Neural Eng.* **13**, 026016 (2016).
15. Duraivel, S. et al. High-resolution neural recordings improve the accuracy of speech decoding. *Nat. Commun.* **14**, 6938 (2023).
16. Khodagholy, D. et al. NeuroGrid: recording action potentials from the surface of the brain. *Nat. Neurosci.* **18**, 310–315 (2015).
17. Steinmetz, N. A. et al. Neuropixels 2.0: a miniaturized high-density probe for stable, long-term brain recordings. *Science* **372**, eabf4588 (2021).
18. Carmena, J. M. et al. Learning to control a brain–machine interface for reaching and grasping by primates. *PLoS Biol.* **1**, e42 (2003).
19. Hochberg, L. R. et al. Reach and grasp by people with tetraplegia using a neurally controlled robotic arm. *Nature* **485**, 372–375 (2012).
20. Gilletti, A. & Muthuswamy, J. Brain micromotion around implants in the rodent somatosensory cortex. *J. Neural Eng.* **3**, 189 (2006).
21. Biran, R., Martin, D. C. & Tresco, P. A. The brain tissue response to implanted silicon microelectrode arrays is increased when the device is tethered to the skull. *J. Biomed. Mater. Res. A* **82A**, 169–178 (2007).
22. Schwarz, D. A. et al. Chronic, wireless recordings of large-scale brain activity in freely moving rhesus monkeys. *Nat. Methods* **11**, 670–676 (2014).
23. Zhou, A. et al. A wireless and artefact-free 128-channel neuromodulation device for closed-loop stimulation and recording in non-human primates. *Nat. Biomed. Eng.* **3**, 15–26 (2018).
24. Topalovic, U. et al. A wearable platform for closed-loop stimulation and recording of single-neuron and local field potential activity in freely moving humans. *Nat. Neurosci.* https://doi.org/10.1038/s41593-023-01260-4 (2023).
25. Oxley, T. J. et al. Minimally invasive endovascular stent-electrode array for high-fidelity, chronic recordings of cortical neural activity. *Nat. Biotechnol.* **34**, 320–327 (2016).
26. Benabid, A. L. et al. An exoskeleton controlled by an epidural wireless brain–machine interface in a tetraplegic patient: a proof-of-concept demonstration. *Lancet Neurol.* **18**, 1112–1122 (2019).
27. Musk, E. An integrated brain-machine interface platform with thousands of channels. *J. Med. Internet Res.* **21**, e16194 (2019).
28. Hariz, M. I. Complications of deep brain stimulation surgery. *Mov. Disord.* **17**, S162–S166 (2002).
29. Jitkritsadakul, O. et al. Systematic review of hardware-related complications of deep brain stimulation: do new indications pose an increased risk? *Brain Stimul.* **10**, 967–976 (2017).
30. Zeng, N. et al. A wireless, mechanically flexible, 25 µm-thick, 65,536-channel subdural surface recording and stimulating microelectrode array with integrated antennas. In *Proc. IEEE Symposium on VLSI Technology and Circuits* 1–2 (IEEE, 2023).
31. Harrison, R. R. & Charles, C. A. low-power, low-noise CMOS amplifier for neural recording applications. *IEEE J. Solid-State Circuits* **38**, 958–965 (2003).
32. Zhang, M. et al. Wireless compact neural interface for freely moving animal subjects: a review on wireless neural interface SoC designs. *IEEE Solid-State Circuits Mag.* **15**, 20–29 (2023).
33. Weiland, J. D., Anderson, D. J. & Humayun, M. S. In vitro electrical properties for iridium oxide versus titanium nitride stimulating electrodes. *IEEE Trans. Biomed. Eng.* **49**, 1574–1579 (2002).
34. Raducanu, B. C. et al. Time multiplexed active neural probe with 1n356 parallel recording sites. *Sensors* **17**, 2388 (2017).
35. *IEEE Standard for Safety Levels with Respect to Human Exposure to Radio Frequency Electromagnetic Fields, 3 kHz to 300 GHz* (IEEE, 2006).
36. Thimot, J. & Shepard, K. L. Bioelectronic devices: wirelessly powered implants. *Nat. Biomed. Eng.* **1**, 0051 (2017).
37. Kim, S., Tathireddy, P., Normann, R. A. & Solzbacher, F. Thermal impact of an active 3-D microelectrode array implanted in the brain. *IEEE Trans. Neural Syst. Rehabil. Eng.* **15**, 493–501 (2007).
38. Marblestone, A. H. et al. Physical principles for scalable neural recording. *Front. Comput. Neurosci.* **7**, 137 (2013).
39. Craner, S. L. & Ray, R. H. Somatosensory cortex of the neonatal pig. I. Topographic organization of the primary somatosensory cortex (SI). *J. Comp. Neurol.* **306**, 24–38 (1991).

40. Okada, Y., Lähteenmäki, A. & Xu, C. Comparison of MEG and EEG on the basis of somatic evoked responses elicited by stimulation of the snout in the juvenile swine. *Clin. Neurophysiol.* **110**, 214–229 (1999).
41. Sauleau, P., Lapouble, E., Val-Laillet, D. & Malbert, C. H. The pig model in brain imaging and neurosurgery. *Animal* **3**, 1138–1151 (2009).
42. van der Maaten, L. aurens & Hinton, G. Visualizing data using *t*-SNE. *J. Mach. Learn. Res.* **9**, 2579 (2008).
43. Pollmann, E. H. et al. A subdural CMOS optical device for bidirectional neural interfacing. *Nat. Electron.* **7**, 829–841 (2024).
44. Mitra, P. P. & Pesaran, B. Analysis of dynamic brain imaging data. *Biophys. J.* **76**, 691–708 (1999).
45. Stavisky, S. D., Kao, J. C., Nuyujukian, P., Ryu, S. I. & Shenoy, K. V. A high performing brain–machine interface driven by low-frequency local field potentials alone and together with spikes. *J. Neural Eng.* **12**, 036009 (2015).
46. Thomson, D. J. Spectrum estimation and harmonic analysis. *Proc. IEEE* **70**, 1055–1096 (1982).
47. Wold, S., Sjöström, M. & Eriksson, L. PLS-regression: a basic tool of chemometrics. *Chemom. Intell. Lab. Syst.* **58**, 109–130 (2001).
48. Das, A., Zabeh, E., Ermentrout, B. & Jacobs, J. Planar, spiral, and concentric traveling waves distinguish cognitive states in human memory. Preprint at *bioRxiv* https://doi.org/10.1101/2024.01.26.577456 (2024).
49. Zabeh, E., Foley, N. C., Jacobs, J. & Gottlieb, J. P. Beta traveling waves in monkey frontal and parietal areas encode recent reward history. *Nat. Commun.* **14**, 5428 (2023).
50. Deng, J. et al. ImageNet: a large-scale hierarchical image database. In *Proc. IEEE Conference on Computer Vision and Pattern Recognition* 248–255 (IEEE, 2009).
51. Willeke, K. F. et al. Deep learning-driven characterization of single cell tuning in primate visual area V4 unveils topological organization. Preprint at *bioRxiv* https://doi.org/10.1101/2023.05.12.540591 (2023).
52. Jia, X., Tanabe, S. & Kohn, A. Gamma and the coordination of spiking activity in early visual cortex. *Neuron* **77**, 762–774 (2013).
53. Woo, S. et al. ConvNeXt V2: co-designing and scaling ConvNets with masked autoencoders. In *Proc. IEEE/CVF Conference on Computer Vision and Pattern Recognition* 16133–16142 (IEEE, 2023).
54. Pierzchlewicz, P. et al. Energy guided diffusion for generating neurally exciting images. *Adv. Neural Inf. Process. Syst.* **36**, 32574–32601 (2023).
55. Cadena, S. A. et al. Diverse task-driven modeling of macaque V4 reveals functional specialization towards semantic tasks. *PLOS Comp. Biol.* **20**, e1012056 (2024).
56. Walker, E. Y. et al. Inception loops discover what excites neurons most using deep predictive models. *Nat. Neurosci.* **22**, 2060–2065 (2019).
57. Fu, J. et al. Pattern completion and disruption characterize contextual modulation in mouse visual cortex. Preprint at *bioRxiv* https://doi.org/10.1101/2023.03.13.532473 (2023).
58. Franke, K. et al. State-dependent pupil dilation rapidly shifts visual feature selectivity. *Nature* **610**, 128–134 (2022).
59. Cowley, B. R., Stan, P. L., Pillow, J. W. & Smith, M. A. Compact deep neural network models of visual cortex. Preprint at *bioRxiv* https://doi.org/10.1101/2023.11.22.568315 (2023).
60. Bashivan, P., Kar, K. & DiCarlo, J. J. Neural population control via deep image synthesis. *Science* **364**, eaav9436 (2019).
61. Zhang, H., Watrous, A. J., Patel, A. & Jacobs, J. Theta and alpha oscillations are traveling waves in the human neocortex. *Neuron* **98**, 1269–1281.e1264 (2018).
62. Das, A. et al. Spontaneous neuronal oscillations in the human insula are hierarchically organized traveling waves. *eLife* **11**, e76702 (2022).
63. Ohki, K. et al. Highly ordered arrangement of single neurons in orientation pinwheels. *Nature* **442**, 925–928 (2006).
64. Kara, P. & Boyd, J. D. A micro-architecture for binocular disparity and ocular dominance in visual cortex. *Nature* **458**, 627–631 (2009).
65. Willett, F. R. et al. A high-performance speech neuroprosthesis. *Nature* **620**, 1031–1036 (2023).
66. Metzger, S. L. et al. A high-performance neuroprosthesis for speech decoding and avatar control. *Nature* **620**, 1037–1046 (2023).
67. Sokal, N. O. & Sokal, A. D. Class E—a new class of high-efficiency tuned single-ended switching power amplifiers. *IEEE J. Solid-State Circuits* **10**, 168–176 (1975).
68. Lim, Y., Tang, H., Lim, S. & Park, J. An adaptive impedance-matching network based on a novel capacitor matrix for wireless power transfer. *IEEE Trans. Power Electron.* **29**, 4403–4413 (2014).
69. Ferro, M. D. & Melosh, N. A. Electronic and ionic materials for neurointerfaces. *Adv. Funct. Mater.* **28**, 1704335 (2018).
70. Jung, T. et al. klshepard/bisc: bioelectronic interface system to the cortex (a wireless subdural-contained 65,536-electrode, 1,024-channel brain-computer interface). *Zenodo* https://doi.org/10.5281/zenodo.17074065 (2025).
71. Calabrese, E. et al. A diffusion tensor MRI atlas of the postmortem rhesus macaque brain. *Neuroimage* **117**, 408–416 (2015).
72. Bakker, R., Tiesinga, P. & Kötter, R. The Scalable Brain Atlas: instant web-based access to public brain atlases and related content. *Neuroinformatics* **13**, 353–366 (2015).

Acknowledgements

This work was partly supported by the Defense Advanced Research Project Agency (DARPA) under contract number N66001-17-C-4001, the Department of the Defense Congressionally Directed Medical Research Program under contract number HT9425-23-1-0758, the National Science Foundation under grant number 1546296 and the National Institutes of Health under grant number R01DC019498. We acknowledge the use of facilities and instrumentation at the Columbia Nano Initiative, the CUNY ASRC and the UPenn Quattrone Nanofabrication Facility. We also thank Y. Borisenkov, A. Banees and K. Kim at Columbia University for help with chip processing and many helpful discussions.

Author contributions

K.L.S., N.Z., T.J. and R.J.C. conceived the project. N.Z., T.J., G.E., M.S., K.T., G.R., Y.H., K.L.S. and R.J.C. designed the implant circuitry. J.D.F., J.K. and H.Y. post-processed the implant. N.Z. and T.J. implemented the relay station hardware. G.E., N.Z., P.M., R.J.C., S.P., T.J., A.M. and L.P.C. implemented the relay station software. T.J., N.Z., J.D.F. and S.P. performed the bench-top characterizations. B.Y., E.S., T.J., N.Z., K.L.S., R.H., I.G. and G.E. performed the in vivo experiments on the porcine subject. T.J., B.Y. and P.C. conducted the porcine data analysis and histology. B.P., A. Dubey, K.E.W., N.Z. and T.J. performed the in vivo experiments on the motor cortex of the NHP. T.J., B.P. and K.E.W. performed the motor cortex data analysis. A.T., S.P., K.L.S., R.J.C., T.J., N.Z., G.E., T.S., G.J.R. and C.N. performed the in vivo experiments on the visual cortex of the NHP. Z.L., K.W., A.T., S.P., D.O., R.J.C., E.Z., A. Das and J.J. performed the visual cortex data analysis. K.L.S., A.T., B.P., M.R., J.J. and D.Y. acquired the funding. K.L.S., A.T., B.Y., B.P., R.J.C., L.P.C. and J.J. provided supervision. T.J., N.Z., J.D.F., G.E., K.L.S., Z.L., K.W., A.T., A. Das, E.Z., J.J. and S.P. wrote the paper with review and editing contributed by all authors.

Competing interests

N.Z. is a principal with Kampto Neurotech, LLC, which is commercializing the BISC technology. The BISC technology is

patented under US patent 11617890, issued on 4 April 2023, and exclusively licensed to Kampto from Columbia University. The other authors declare no competing interests.

Additional information

Extended data is available for this paper at https://doi.org/10.1038/s41928-025-01509-9.

Supplementary information The online version contains supplementary material available at https://doi.org/10.1038/s41928-025-01509-9.

Correspondence and requests for materials should be addressed to Andreas Tolias or Kenneth L. Shepard.

Peer review information *Nature Electronics* thanks the anonymous reviewers for their contribution to the peer review of this work.

Taesung Jung[1,26], Nanyu Zeng[1,2,26], Jason D. Fabbri[1], Guy Eichler[3], Zhe Li[4,5,6], Erfan Zabeh[7], Anup Das[7], Konstantin Willeke[4,5,6,8], Katie E. Wingel[9,10], Agrita Dubey[9,10], Rizwan Huq[1], Mohit Sharma[1], Yaoxing Hu[1], Girish Ramakrishnan[1], Kevin Tien[1], Paolo Mantovani[3], Abhinav Parihar[1], Heyu Yin[1], Denise Oswalt[10,11,12], Alexander Misdorp[3], Ilke Uguz[1], Tori Shinn[13], Gabrielle J. Rodriguez[4,5,6], Cate Nealley[4,5,6], Tjitse van der Molen[14,15], Sophia Sanborn[5,6], Ian Gonzales[16], Michael Roukes[17,18,19], Jeffrey Knecht[20], Kenneth S. Kosik[14,15], Daniel Yoshor[10], Peter Canoll[21], Eleonora Spinazzi[16], Luca P. Carloni[3], Bijan Pesaran[9,10,11,12], Saumil Patel[4,5,6], Joshua Jacobs[22], Brett Youngerman[16], R. James Cotton[23,24], Andreas Tolias[4,5,6,13,25] ✉ & Kenneth L. Shepard[1,7,16] ✉

[1]Department of Electrical Engineering, Columbia University, New York, NY, USA. [2]Kampto Neurotech LLC, Troy, NY, USA. [3]Department of Computer Science, Columbia University, New York, NY, USA. [4]Department of Ophthalmology, Byers Eye Institute, Stanford University, Stanford, CA, USA. [5]Stanford Bio-X, Stanford University, Stanford, CA, USA. [6]Wu Tsai Neurosciences Institute, Stanford University, Stanford, CA, USA. [7]Department of Biomedical Engineering, Columbia University, New York, NY, USA. [8]Institute of Computer Science and Campus Institute Data Science, University of Göttingen, Göttingen, Germany. [9]Center for Neural Science, New York University, New York, NY, USA. [10]Department of Neurosurgery, University of Pennsylvania, Philadelphia, PA, USA. [11]Department of Neuroscience, University of Pennsylvania, Philadelphia, PA, USA. [12]Department of Bioengineering, University of Pennsylvania, Philadelphia, PA, USA. [13]Center for Neuroscience and Artificial Intelligence, Department of Neuroscience, Baylor College of Medicine, Houston, TX, USA. [14]Neuroscience Research Institute, University of California Santa Barbara, Santa Barbara, CA, USA. [15]Department of Molecular, Cellular and Developmental Biology, University of California Santa Barbara, Santa Barbara, CA, USA. [16]Department of Neurological Surgery, Columbia University, New York, NY, USA. [17]Department of Applied Physics, Caltech, Pasadena, CA, USA. [18]Department of Physics, Caltech, Pasadena, CA, USA. [19]Department of Bioengineering, Caltech, Pasadena, CA, USA. [20]Lincoln Laboratory, Massachusetts Institute of Technology, Lexington, MA, USA. [21]Department of Pathology and Cell Biology, Columbia University, New York, NY, USA. [22]Department of Neurology and Neuroscience Institute, University of Chicago, Chicago, IL, USA. [23]Shirley Ryan Ability Labs, Chicago, IL, USA. [24]Department of Physical Medicine and Rehabilitation, Northwestern University, Chicago, IL, USA. [25]Department of Electrical Engineering, Stanford University, Stanford, CA, USA. [26]These authors contributed equally: Taesung Jung, Nanyu Zeng. ✉e-mail: tolias@stanford.edu; shepard@ee.columbia.edu

https://doi.org/10.1038/s41928-025-01509-9

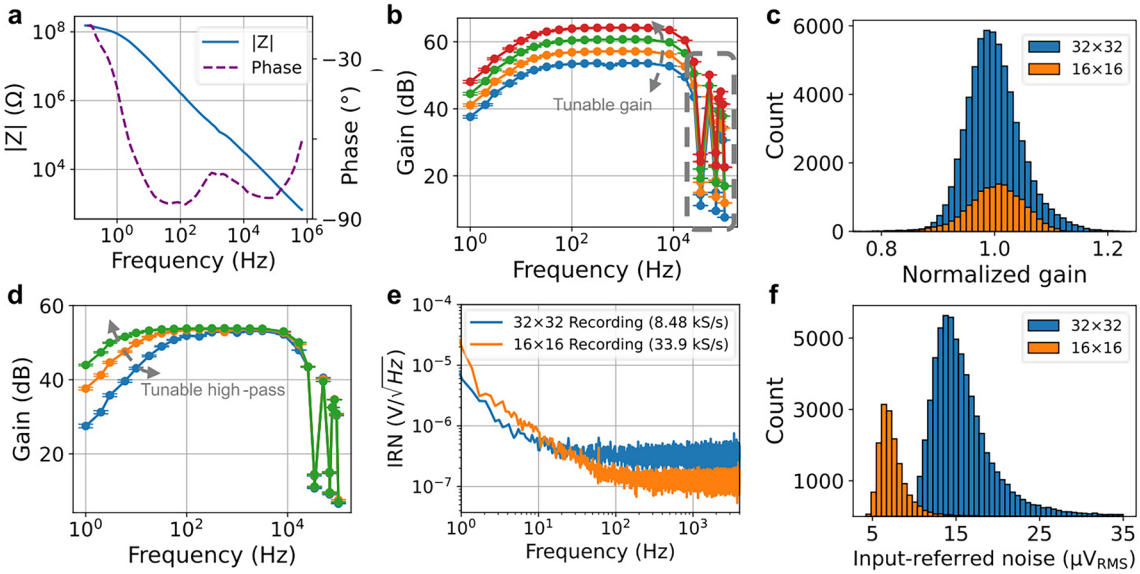

Extended Data Fig. 1 | Bench-top in vitro characterization of the BISC implant. (**a**) Electrochemical impedance spectroscopy of titanium nitride electrode. (**b**) Frequency response across different gain configurations from a representative 16×16 recording. Note that gain is programmed through a single back-end amplifier that is shared by all pixels. Error bars indicate standard error (SE), and dashed rectangle marks the effects of boxcar sampling (flat band gains: 53.7 ± 0.20 dB, 57.2 ± 0.21 dB, 60.7 ± 0.20 dB, 64.2 ± 0.19 dB, values: mean ± SD. n = 255, 255, 245, 235). (**c**) Histogram of normalized channel gain variation for each recording mode (16×16 mode: 100 ± 5.1%, 32×32 mode: 100 ± 4.8%, values: mean ± SD. n = 15,163 and 62,245). (**d**) Frequency response across different high-pass (HP) filter configurations from a representative 16×16 recording. Error bars indicate SE (3-dB corner: 4.19 ± 2.28 Hz, 13.30 ± 2.37 Hz, 54.42 ± 1.98 Hz, values: mean ± SD. n = 244, 254, 256). (**e**) Input-referred noise (IRN) spectrum averaged over representative pixels (n = 10) for each recording mode. (**f**) Histogram of channel IRN for each recording mode, integrated from 10 Hz to 4 kHz (16×16 mode: 7.68 ± 3.11 μV_{RMS}, 32×32 mode: 16.51 ± 6.85 μV_{RMS}, values: mean ± SD. n = 15,163 and 62,245).

https://doi.org/10.1038/s41928-025-01509-9

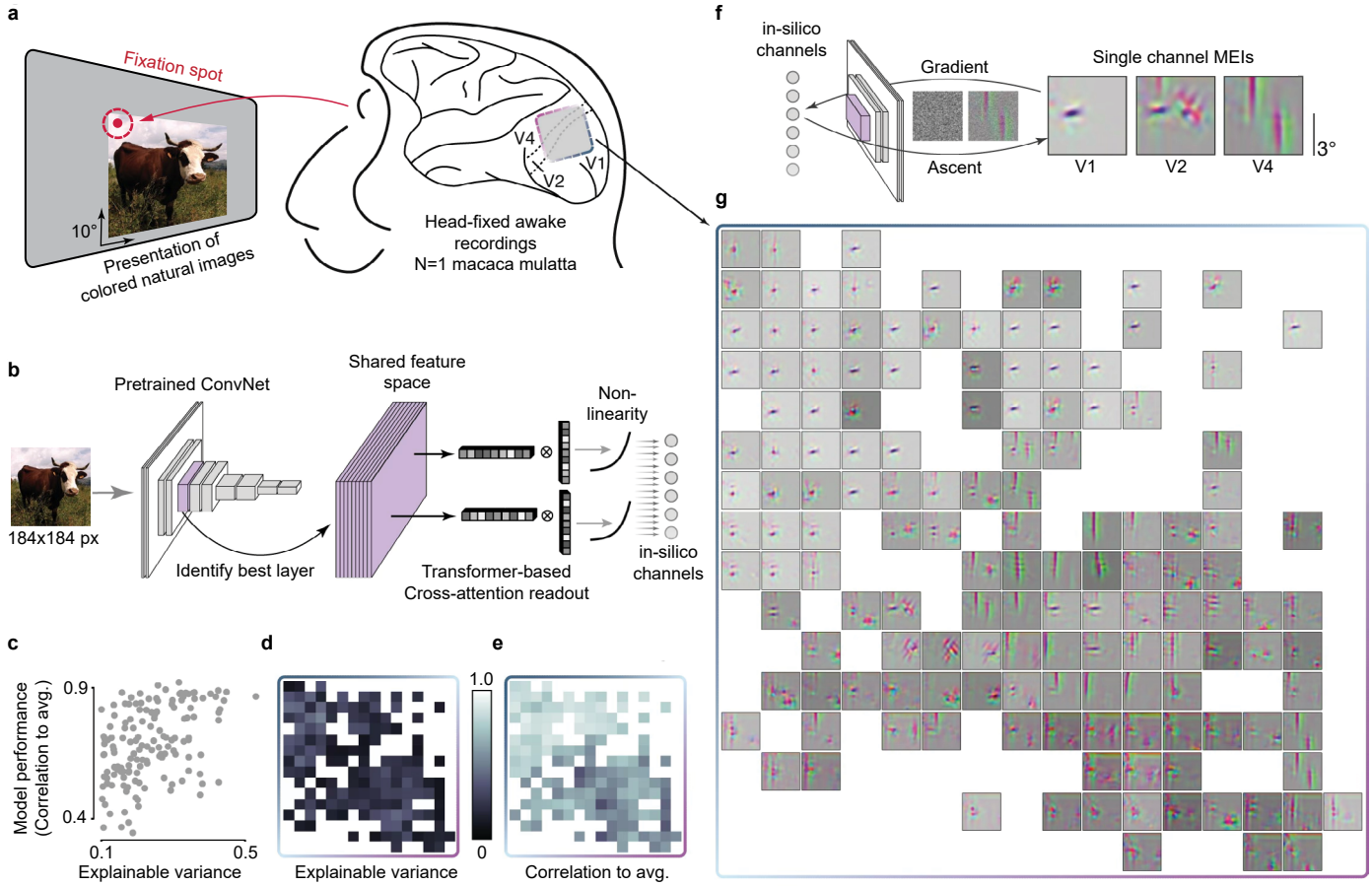

Extended Data Fig. 2 | BISC recordings over visual cortex with natural images. (**a**) We presented static colored natural images, while the monkey maintained fixation (120 ms presentation time per image, 15 images per trial, 1200 ms inter-trial period). Each image (10°×10°) was centered 3° to the right and below the fixation spot. (**b**) Model architecture: Pre-processed stimuli (184 × 184 pixels) and neuronal responses were used to train a neural predictive model, which takes images as an input and outputs an estimate of the underlying neuronal activity. We passed the images through a ConvNext model, pre-trained on an image classification task to obtain image embeddings, that is a shared feature space. We then computed the neuronal responses by passing the feature activations through a transformer-based readout followed by a non-linearity stage. (**c**) Explainable variance, a measure of response reliability to natural images, plotted against the model's predictive performance (correlation between prediction and average neural response to repeated presentations) of all 144 channels (explainable variance 0.24 ± 0.09, and correlation to average 0.69 ± 0.14. values: mean ± SD). Only channels with an explainable variance greater than or equal to 0.1 are included in these analyses. (**d**) Spatial map of explainable variance across the recording array (same layout as in Fig. 4 and Fig. 5e). (**e**) Same as (**d**), but showing the model's predictive performance (correlation to average neural response). (**f**) Schematic illustrating optimization of maximally exciting images (MEIs). A random starting image was iteratively optimized to elicit maximal activity for each in-silico channel, revealing the visual features to which that channel is selective. Three example MEIs from areas V1, V2, and V4 are shown. (**g**) MEIs for all 144 channels across the array which reliably responded to repeated image presentations. MEIs in area V1 are characterized by oriented Gabor filters, while the channels overlying area V2 and V4 exhibit more complex, color opponent feature tuning. Credit: cow image in **a**,**b**, Nicolas Vigier, flickr under a Creative Commons license CC0.

nature portfolio

Corresponding author(s): Andreas Tolias, Kenneth L. Shepard

Last updated by author(s): Oct 12, 2025

Reporting Summary

Nature Portfolio wishes to improve the reproducibility of the work that we publish. This form provides structure for consistency and transparency in reporting. For further information on Nature Portfolio policies, see our Editorial Policies and the Editorial Policy Checklist.

Statistics

For all statistical analyses, confirm that the following items are present in the figure legend, table legend, main text, or Methods section.

n/a	Confirmed	
☐	☒	The exact sample size (*n*) for each experimental group/condition, given as a discrete number and unit of measurement
☒	☐	A statement on whether measurements were taken from distinct samples or whether the same sample was measured repeatedly
☐	☒	The statistical test(s) used AND whether they are one- or two-sided *Only common tests should be described solely by name; describe more complex techniques in the Methods section.*
☒	☐	A description of all covariates tested
☒	☐	A description of any assumptions or corrections, such as tests of normality and adjustment for multiple comparisons
☐	☒	A full description of the statistical parameters including central tendency (e.g. means) or other basic estimates (e.g. regression coefficient) AND variation (e.g. standard deviation) or associated estimates of uncertainty (e.g. confidence intervals)
☐	☒	For null hypothesis testing, the test statistic (e.g. *F*, *t*, *r*) with confidence intervals, effect sizes, degrees of freedom and *P* value noted *Give P values as exact values whenever suitable.*
☒	☐	For Bayesian analysis, information on the choice of priors and Markov chain Monte Carlo settings
☒	☐	For hierarchical and complex designs, identification of the appropriate level for tests and full reporting of outcomes
☐	☒	Estimates of effect sizes (e.g. Cohen's *d*, Pearson's *r*), indicating how they were calculated

Our web collection on statistics for biologists contains articles on many of the points above.

Software and code

Policy information about availability of computer code

Data collection	Custom codes used to collect the data in this study are available from the corresponding authors upon reasonable request
Data analysis	Custom codes used to analyze the data in this study are available at https://github.com/klshepard/bisc

For manuscripts utilizing custom algorithms or software that are central to the research but not yet described in published literature, software must be made available to editors and reviewers. We strongly encourage code deposition in a community repository (e.g. GitHub). See the Nature Portfolio guidelines for submitting code & software for further information.

Data

Policy information about availability of data

All manuscripts must include a data availability statement. This statement should provide the following information, where applicable:

- Accession codes, unique identifiers, or web links for publicly available datasets
- A description of any restrictions on data availability
- For clinical datasets or third party data, please ensure that the statement adheres to our policy

Data supporting the findings of this study are available at https://zenodo.org/records/17074065 (doi.org/10.5281/zenodo.17074064)

Research involving human participants, their data, or biological material

Policy information about studies with human participants or human data. See also policy information about sex, gender (identity/presentation), and sexual orientation and race, ethnicity and racism.

Reporting on sex and gender	Not applicable to our study
Reporting on race, ethnicity, or other socially relevant groupings	Not applicable to our study
Population characteristics	Not applicable to our study
Recruitment	Not applicable to our study
Ethics oversight	Not applicable to our study

Note that full information on the approval of the study protocol must also be provided in the manuscript.

Field-specific reporting

Please select the one below that is the best fit for your research. If you are not sure, read the appropriate sections before making your selection.

☒ Life sciences ☐ Behavioural & social sciences ☐ Ecological, evolutionary & environmental sciences

For a reference copy of the document with all sections, see nature.com/documents/nr-reporting-summary-flat.pdf

Life sciences study design

All studies must disclose on these points even when the disclosure is negative.

Sample size	Not applicable to our study
Data exclusions	From our multi-channel electrophysiological recordings, we excluded data from channels that do not meet our recording fidelity criteria. These criteria and procedures have been described in detail in Supplementary Discussions S6 (Porcine somatosensory cortex recording data analysis), S8 (NHP motor cortex recording data analysis), and S10 (NHP visual cortex recording data analysis)
Replication	Not applicable to our study
Randomization	Not applicable to our study
Blinding	Not applicable to our study

Reporting for specific materials, systems and methods

We require information from authors about some types of materials, experimental systems and methods used in many studies. Here, indicate whether each material, system or method listed is relevant to your study. If you are not sure if a list item applies to your research, read the appropriate section before selecting a response.

Materials & experimental systems

n/a	Involved in the study
☐	☒ Antibodies
☒	☐ Eukaryotic cell lines
☒	☐ Palaeontology and archaeology
☐	☒ Animals and other organisms
☒	☐ Clinical data
☒	☐ Dual use research of concern
☒	☐ Plants

Methods

n/a	Involved in the study
☒	☐ ChIP-seq
☒	☐ Flow cytometry
☒	☐ MRI-based neuroimaging

Antibodies

Antibodies used	Iba1 (Novus Biologicals, NB100-1028) NeuN (Millopore, MAB377)

Validation	Iba1 and NeuN have been validated for immunohistochemistry on pigs Manufacture websites: https://www.novusbio.com/products/aif-1-iba1-antibody_nb100-1028 https://www.emdmillipore.com/US/en/product/Anti-NeuN-Antibody-clone-A60,MM_NF-MAB377

Animals and other research organisms

Policy information about studies involving animals; ARRIVE guidelines recommended for reporting animal research, and Sex and Gender in Research

Laboratory animals	Our study used one porcine subject (Yorkshire pig, 18 weeks old), one non-human primate subject for investigating motor cortex (Macaca mulatta, 11 years old), one non-human primate subject for investigating visual cortex (Macaca mulatta, 19 years old)
Wild animals	Not applicable to our study
Reporting on sex	Not applicable to our study
Field-collected samples	Not applicable to our study
Ethics oversight	Study on the porcine model: Columbia Univerisity IACUC #AC-AABQ0559 Study on the non-human primate for investigating motor cortex: New York University IACUC and University of Pennsylvania IACUC #807341 Study on the non-human primate for investigating visual cortex: Baylor College of Medicine IACUC #AN-4367

Note that full information on the approval of the study protocol must also be provided in the manuscript.

Plants

Seed stocks	Not applicable to our study
Novel plant genotypes	Not applicable to our study
Authentication	Not applicable to our study